THE EUROPEAN
PHYSICAL JOURNAL A

# Results and plans for nuclear spectroscopy of superheavy nuclei: the Lund perspective

**D. Rudolph**[a] (iD)

Department of Physics, Lund University, 22100 Lund, Sweden

**Abstract** A survey of nuclear structure results obtained along $\alpha$-decay chains stemming from isotopes of element 114, Fl, and element 115, Mc, is presented. Measures taken to ensure a reliable hand-over of nuclear spectroscopy output to nuclear structure theory are outlined. Possible links between decay chains starting from element 117, Ts, and element 115, Mc, are commented on. The experiments were conducted with the TASISpec set-up placed in the focal plane of the TASCA separator at the GSI Helmholtzzentrum für Schwerionenforschung GmbH in Darmstadt, Germany. Plans to improve the decay-spectroscopy set-up towards future superheavy endeavours are described.

## 1 Introduction

In the wake of the discovery of new superheavy elements, nuclear spectroscopy experiments aim at providing benchmarks for nuclear structure theory at the uppermost end of the nuclear chart. A central and long-standing question concerns nuclear binding or nuclear stability of superheavy nuclei. This relates to the underlying nuclear shell structure, i.e., the evolution of the nuclear shell structure as a function of, for example, proton and neutron number. In other words: What is the next (spherical) doubly-magic nucleus beyond $^{208}$Pb?

By 1969 elements up to $Z = 104$ had been discovered experimentally. Calculations by, for instance, nuclear theorist Sven Gösta Nilsson and collaborators in Lund described a superheavy 'Island of Stability' around nuclei with proton number $Z = 114$ and neutron number $N = 184$ [1]. Calculations by Meyers and Swiatecki [2] as well as Mosel and Greiner [3] had provided similar predictions. By the year 2000 elements up to $Z = 116$ and $N = 176$ had been discovered in experiments and a new class of nuclear models based on nuclear density-functional theory started to make predic-

tions for how heavy elements that can exist [4,5]. This new class of models has indicated the importance of density redistribution effects that can move the energy gaps in the nuclear spectra. One such effect is that the electrostatic repulsion between the protons can form a region of reduced density in the centre of the nucleus that can lead to decisive changes in the spectra. Owing to this interplay of subtle effects, a more nuanced picture has emerged where models that make similar predictions for lighter nuclei differ in the predictions of heavy or superheavy nuclei (see, e.g., [6,7] and references therein). Further, the inclusion of beyond mean-field methods can probe deformation softness or shape coexistence in the full $\beta-\gamma$ plane [8–10].

As a consequence, to avoid extrapolations over some 30 or so mass units, the experimental task is to provide theory with spectroscopic data to probe their models or model parametrisations at or near element $Z = 114$, flerovium. Interesting quantities are precise $Q_\alpha$ values and the corresponding decay times. Another crucial piece of data concerns $\gamma$ and X-ray radiation that can be emitted following an $\alpha$-decay. Since the X-ray energies are characteristic for the different elements [11] they can provide confirmation of the proton number of the nucleus being studied and, hence, the chemical element [12]. The $\gamma$ rays on the other hand give access to spectral properties of the nuclei and inform us about their internal nuclear structure. For nuclei with odd particle numbers it is essential to evaluate the $\alpha$ decays to different excited states of the daughter nucleus in order to determine if the daughter will be left in an excited state. It is for such cases that one has a chance of observing the subsequent electromagnetic decay providing us with in-depth information *directly* on the heaviest elements. Figuratively speaking, the idea is to convert the discovery-related $\alpha$-decay squares on the chart of nuclei (see, e.g., [13–15] and references therein) into decay schemes which carry crucial information to improve the description of the strong force in the heaviest nuclear systems.

[a] e-mail: Dirk.Rudolph@nuclear.lu.se (corresponding author)

The main experimental challenge is posed by the tiny production and thus observation rates. Therefore, it is of utmost importance to have a spectroscopy set-up capable of comprehensively measuring $\alpha$ decays, $\gamma$ rays, $x$ rays, as well as electrons from internal conversion in coincidence, with high efficiency, and with low energy thresholds. In Sect. 2, the TASISpec set-up developed in Lund is described [16], together with a reminder of spectroscopic tools used and applied to ensure high-quality spectroscopic data handed over to nuclear theory. Sections 3 and 4 review the main results of the spectroscopy experiments conducted on element 114, flerovium, and element 115, moscovium. Based on the latter, suggestions for linking decay chains associated with isotopes of moscovium and tennessine are presented in Sect. 5. This is followed in Sect. 6 by an outlook toward a novel decay station being prepared in Lund, named LUNDIUM . A brief summary concludes this contribution.

## 2 Experimental and spectroscopic tools

The activities of the Lund group have been largely embedded in the superheavy element research programme at the GSI Helmholtzzentrum für Schwerionenforschung in Darmstadt, Germany, and more recently also in the frame of FAIR Phase-0. Both commissioning, preparatory, and the two main experiments aimed at spectroscopy of decay chains stemming from isotopes of flerovium and moscovium, respectively, were conducted in the focal plane of the gas-filled TransActinide Separator and Chemistry Apparatus (TASCA) [17,18]. The idea of a compact cube of silicon strip detectors for detection of implantation and charged-particle decays of (super)heavy nuclei, surrounded by large composite germanium detectors for highly efficient coincidence measurements with $\gamma$ rays or $x$ rays, had its origin in the so-called small-image mode of TASCA – hence the acronym TASISpec, TASCA Small-Image mode Spectroscopy. Figure 1 shows a photograph of the 'silicon cube' of TASISpec. For more information on TASISpec in general see [16]. Further TASISpec details for either of the two main experiments can be found in the PhD theses of Forsberg [20] and Såmark-Roth [21], respectively.

During TASCA and TASISpec commissioning runs, it had turned out that background in the focal plane reduced significantly more for high-transmission than small-image mode settings of TASCA. Though this implied a minor loss in measured [22] and simulated [23] TASCA transmission into TASISpec, detector rate and spectral quality were judged more important. Specific TASISpec focussing schemes, which involve asymmetric settings of the two TASCA quadrupole magnets [17], were then tested and established [20,22].

The experimental concepts of TASISpec and applied data-analysis techniques are similar to those outlined for
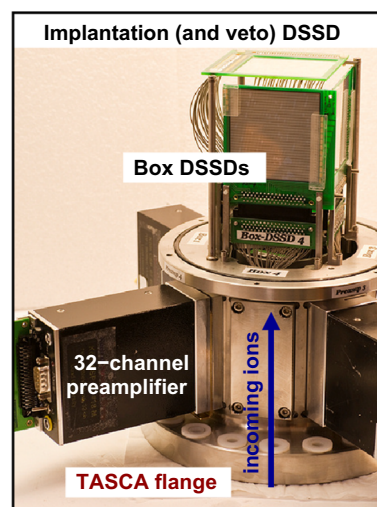


**Fig. 1** Photograph of the silicon-detector cube of TASISpec as used for the 'element 115 experiment' in 2012. Mounted directly at the focal plane of TASCA, superheavy ions can reach the cube through a (hidden) tube of 70 mm diameter. Implantation and charged-particle decays are registered in the DSSD seen on top of the picture. Particles emitted from the implantation spot into beam direction can be caught by four box DSSDs. Miniature 50-$\Omega$ coaxial cables guide the detector signals to 32-channel preamplifiers [19] which are directly connected to the TASISpec chamber. For the 'element 114 experiment' in 2019/2020, a sixth DSSD was positioned right behind the implantation DSSD to veto $\beta$-decay events and other types of radioactive background. All DSSD are $60 \times 60$ mm$^2$ in size and have 32 strips on each side, i.e., a nominal pixelation of 1024. Two adjacent strips are combined for box detectors, reducing this number to 256 for each box DSSD. During experiments, the DSSD cube is surrounded by a 0.5–1.0 mm thin aluminium housing, and each DSSD is backed by a composite germanium detector of 4-crystal clover and/or 7-crystal cluster type [16]

other decay stations focussing on multi-coincidence high-resolution decay spectroscopy in recent or this Topical Issue on heavy and superheavy nuclei (see, e.g., [24–27] and references therein). TASISpec was one of the first decay stations to be upgraded into a fully pixelated system of double-sided silicon strip detectors (DSSDs) (cf. Fig. 1). This enables tracking $\alpha$-decay particles (or fission fragments) leaving the implantation DSSD and reaching one of the box DSSDs. Once dead-layer thicknesses of the two engaged pixels are known, decay energies can be reconstructed with almost as good resolution as if the $\alpha$ particle had moved deeper into the implantation DSSD. Relevant dead-layer scans were conducted for all TASISpec DSSD with standard $\alpha$ and electron radioactive sources [20,28].

TASISpec was also one of the first decay stations to employ digital electronics, i.e., to directly register the output signals of the preamplifiers in typically 70–80 $\mu$s long traces at 50–60 MHz and 12–14-bit depth. Developed at the GSI-EE Department, 16-channel FEBEX3 modules were used. Early on, this by now common way of digitization had been done solely for the 32 p-side channels of the implanta-

tion DSSD, later-on for all DSSD strips, up to 256 in total, and more recently also for the germanium detector crystals, the latter with more elaborate FEBEX4 hardware and firmware. Inspecting these traces has a multitude of advantages compared with standard analog electronics. One of specific relevance for decay chains originating from flerovium and moscovium, with $\alpha$-decay energies in the interval 9.0–10.5 MeV, is that false candidate events due to fast $\alpha$ emitters from transfer–reaction channels can be readily traced and disregarded immediately: A full-energy $\alpha$ detection in the implantation DSSD of some 8.5–9.5 MeV, preceded or followed by an escape-$\alpha$ pile-up event of some 0.5–1.0 MeV, also deposited in the implantation DSSD and within less than a few microseconds, leads to summing in conventional electronics and could thus be misinterpreted as being part of a superheavy element decay chain (cf. chap. 6 in [20]). In turn, dedicated analysis of such events can reveal new structure information for these transfer–reaction channels [29].

From a spectroscopy perspective, the availability of the preamplifier pulse allows to probe and develop codes for various digital filters in order to optimize the channel-by-channel energy resolution of the DSSDs [20,21,29]. Prior to experiments, energy calibration of the DSSD cube is done with the help of external $\alpha$ and electron standard sources, of course using and cross-checking pixel-by-pixel dead-layer thicknesses. For $\alpha$ decays with energy $E_\alpha$, the energy deposited by the implanted recoil has to be accounted for as well:

$$E_{\text{det}} = E_\alpha \cdot \left( 1 + \frac{4}{A-4} \cdot r \right). \tag{1}$$

A fraction, $r$, of the recoil energy contributes to the detected energy, $E_{\text{det}}$ – unless there is further summing with electrons from coincident internal conversion decay, of course. For the 'element 115 experiment', a constant $r = 0.5$ was used [20]. For the 'element 114 experiment', a more sophisticated study of a number of cases of implanted nuclei produced in preparatory experiments yielded $r = r(Z^2) \approx 0.40 - 0.60$ for $Z \approx 85 - 115$ [21,30]. Either way, the methods were tested on ample known $\alpha$ emitters in the range $E_\alpha \approx 7 - 12$ MeV and found to agree with tabulated values within $< 10$ keV [20,21,29]. Finally, over the period of week-long experiments, electronic gains can drift. Therefore, data was cut into reasonably sized portions and such drifts accounted for if deemed necessary. For this purpose, the modest but notable amount of $\alpha$ decays of transfer-reaction background detected in the focal plane of TASCA proved useful, including events at $E_\alpha = 11.66$ MeV originating from $^{212m}$Po (cf. Fig. 6.9 in [20] and Fig. 3 in [30]).

Simulations – or virtual experiments – using the Geant4 toolkit have entered the nuclear physics domain some time ago. Therefore, TASISpec has been coded in detail in Geant4 [31] while allowing for adoptions in geometry and detector types for a given TASISpec set-up, for instance, for the 'ele-

ment 115 experiment' [32,33]. It is also possible to conduct virtual Geant4 experiments in 'real time' and compare virtual Geant4 data with data taken in real experiments. This feature has proven very helpful for experiments in which TASISpec had been placed behind ion traps, such that the decay of a certain isotope with a given mass, i.e., the decay of a selected single quantum state, could be followed over time [34] – regardless whether that be $\alpha$ decay, $\beta$ decay, or proton emission [35–37]. The most important asset of the Geant4 simulations for superheavy element spectroscopy studies, however, is the capability of self-consistency control of the decay schemes derived from the measured $\alpha$, electron, and photon spectra, as well as coincidences among these (see, e.g., [32,33] and below). Using the decay schemes as physics input for Geant4, virtual experiments provide expected spectra, which within given statistical limits must match the observed ones in order to validate the very same suggested decay scheme. Figures 3 in [32] or [38] provide good examples of both a calibration aspect ($\alpha$-$\gamma$ coincidence in $^{211}$Bi) or discriminating $E1$ or $M1$ character of $\gamma$ rays seen in $^{276}$Mt ($Z = 109$) in coincidence with the $\alpha$ decay of $^{280}$Rg ($Z = 111$). Besides this core feature of Geant4 simulations, they can also prove helpful in specific data assessments. For example, energies and depths of ions entering the implantation DSSD can be studied, in correlation with the partial energy loss of reconstructed $\alpha$-particle events. This can provide additional evidence to disregard a candidate flerovium decay chain and allows to deduce a depth profile of ion implantations (cf. Fig. 5.6 in [21]).

An important facet of the nuclear spectroscopy experiments at GSI, and in particular for those in the focal plane of TASCA, is the 25% duty cycle of the UNILAC, with 5 ms beam on and 15 ms beam off. With TASISpec necessarily placed inside the TASCA experiment cave, nuclear spectroscopy with germanium detectors is hardly possible during beam-on periods due to too high radiation levels. In turn, for most of the time there is no primary beam, which allows for proper decay-spectroscopy measurements. Furthermore, detecting recoil-$\alpha$ correlations as they are recorded online allows to trigger an electrostatic chopper to bend the primary beam off axis in less than 20 $\mu$s. The beam-off periods can then be prolonged as long as needed to detect the remaining part of a superheavy element decay chain in a rather quiet radiation environment. It is noteworthy to point out that the 15-ms beam-off periods can help tremendously in identifying proper initial recoil-$\alpha$ candidates, which was most relevant for the 'element 114 experiment' due to the rather long half-lives of $^{288,289}$Fl, which are on the order of a second.

Finally, hardly any of the above mentioned spectroscopic tools or measures are particularly new or unique for TASISpec. Nevertheless, they should in one way or another be applied to any experiment claiming spectroscopic relevance for superheavy element research.

# 3 Decay chains associated with Fl isotopes

An experiment proposal targeting decay chains stemming from $^{289}$Fl was approved at GSI in 2017. Originally scheduled for summer 2018, it could first be conducted in two parts in 2019 and 2020, respectively, due to accelerator problems. Four out of five COMPEX modules were delivered and used, while the set-up was otherwise a fine-tuned version of TASISpec [30]. More details of the set-up, the experiment itself, and the specific analysis steps and tools are described comprehensively in [21]. In brief, the reaction $^{48}$Ca+$^{244}$Pu was focused upon, while one out of four target segments in 2019 held enriched $^{242}$Pu instead. A total beam integral of $6.0(4) \cdot 10^{18}$ was collected, leading to the observation of 32 flerovium candidate chains. Of these, two were associated with $^{286}$Fl and twelve with $^{288}$Fl [39], as well as fifteen with $N = 175$ $^{289}$Fl [21,40]. Three additional decay chains of possible $^{289}$Fl origin were disregarded because of too much similarity with random background [21,41]. Thus, 29 flerovium decay chains were observed in less than three weeks of beam time, i.e., a little more than ten per week at average beam currents of $4 \cdot 10^{12}$/s at the time. Accounting for target thicknesses of 0.80(1) mg/cm$^2$ $^{244}$Pu, recoil transmission into TASISpec, as well as detection and identification probabilities [21], this corresponds to production cross sections of $\approx 5$ pb for $^{288}$Fl and $^{289}$Fl, respectively. The exact numbers [21,41] agree well with previous measurements summarized in Fig. 11 of [42], and they help to further delineate the shape of the excitation functions for $3n$ and $4n$ evaporation channels.

Turning to admittedly unexpected spectroscopy highlights of the even-even isotopes $^{286,288}$Fl [39], Fig. 2a shows an $\alpha$-decay energy spectrum for the decay step $^{288}$Fl $\rightarrow$ $^{284}$Cn for the 32 previous world-data events, originating from several discovery and confirmation experiments conducted at different facilities [42–49]. To take into account the various uncertainties of individual events, for a single entry, a Gaussian with integral one and a width compliant with its measured uncertainty was added into the spectrum. One may think that the rather broad doublet structure, which in overall shape is at variance with a common ground-state to ground-state $\alpha$ decay line of an even–even nucleus, relates to somewhat different calibrations of the different experiments. However, the puzzling $\approx 100$-keV split [50] was reported independently in all previous experiments, let it be via direct or indirect population of $^{288}$Fl. Figure 2b shows the same spectrum for the twelve chains observed with TASISpec and associated with $^{288}$Fl. The difference in spectroscopic quality is striking, and the above mentioned puzzle is resolved: A single $\alpha$-decay line at 9.92(1) MeV with a full-width at half maximum of 35 keV emerges from eleven available events. This establishes the decay characteristics of $^{288}$Fl to $Q_\alpha = 10.06(1)$ MeV and $T_{1/2} = T_{1/2,\alpha} = 0.65(^{12}_8)$ s, in line with earlier values.
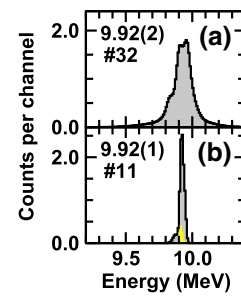


**Fig. 2** Experimental $\alpha$-decay energy spectra from events associated with the decay step $^{288}$Fl $\rightarrow$ $^{284}$Cn. For a single entry, a Gaussian with integral one and a width compliant with its measured uncertainty was added into the respective spectrum. The numbers in the top left of each panel are the $\alpha$-decay energies extracted by computing the histogram mean in the interval [9.3,10.3] MeV. The numbers behind the hashtag, #, indicate the number of available data points. **a** summarizes previous world data, **b** the TASISpec data from 2019 and 2020
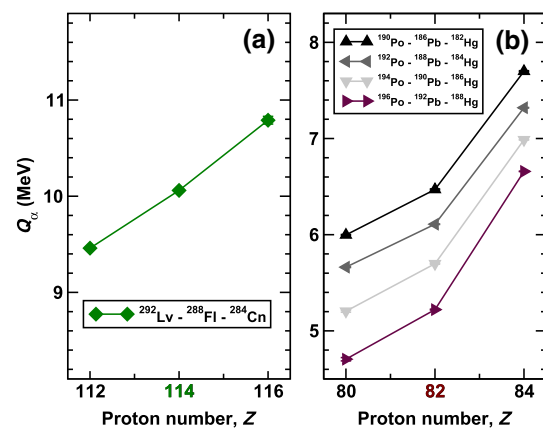


**Fig. 3** **a** $Q_\alpha$ sequence across $Z = 114$, flerovium, at neutron number $N = 174$. **b** Several $Q_\alpha$ sequences across the firm magic number $Z = 82$, lead, about twenty neutrons away from doubly magic $^{208}$Pb

The event plotted in yellow in Fig. 2b marks the decay chain which comprises a second $\alpha$ decay with $E_\alpha = 9.33(1)$ MeV, prior to a fast fission event after only $\Delta t = 518$ $\mu$s. This chain is highlighted in [39] as it marks the first firm full-energy observation of a weak ($\approx 2\%$) $Q_\alpha = 9.46(1)$-MeV decay branch from $^{284}$Cn into $^{280}$Ds. Adding the known $Q_\alpha = 10.79(4)$ MeV for the $^{292}$Lv $\rightarrow$ $^{288}$Fl $\alpha$ decay, a smooth $Q_\alpha$ sequence *across* $Z = 114$ could be experimentally established for the first time. This is illustrated in Fig. 3a and compared with Po-Pb-Hg sequences in Fig. 3b. Note that these sequences cross $Z = 82$ some 20 neutrons away from doubly-magic $^{208}$Pb. Obviously, there is hardly any kink seen for $Z = 114$, while it is characteristic for any pronounced shell gap, i.e., magic numbers, such as the well-known one at $Z = 82$. In essence, that observation rules out all nuclear structure models predicting a distinct magic shell gap at $Z = 114$.

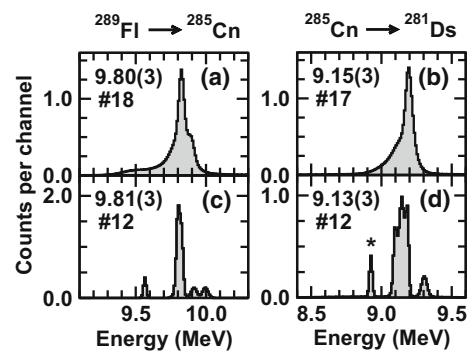The second spectroscopic highlight concerns the observation of an $\alpha$-electron coincidence event in one of the
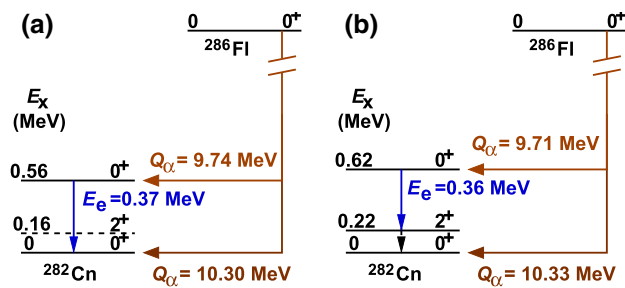
Fig. 4 Two decay scenarios involving the excited state at $E_x \approx$ 0.6 MeV in $^{282}$Cn populated via the $^{286}$Fl $\alpha$ decay. The transitions associated with the measured $E_e = 0.36(1)$ MeV electron are marked in blue; they originate from a K-converted $E0$ transition in **a** or an L-converted $E2$ transition in **b**



Fig. 5 Experimental decay-energy spectra from events associated with the decay steps $^{289}$Fl $\rightarrow ^{285}$Cn (left column) and $^{285}$Cn $\rightarrow ^{281}$Ds (right column). For a single entry, a Gaussian with integral one and a width compliant with its measured uncertainty was added into the respective spectrum. The numbers at the top left of each panel are the ($\alpha$-decay) energies extracted by computing the histogram mean in the interval [9.4,10.2] MeV (left panels) and [8.6,9.6] MeV (right panels), respectively. For all four panels, the number after the hashtag, #, indicates the number of available data points. The top row refers to all previously, directly or indirectly, observed $^{289}$Fl or $^{285}$Cn decays, respectively. The bottom row shows a compilation of the events measured with TASISpec [21,40]

two decay chains starting from $^{286}$Fl [39]. Since the $E_e =$ 0.36(1)-MeV conversion electron [21,41] was detected in one of the box DSSD, the detected $E = 9.60(1)$ MeV in the implantation DSSD likely corresponds to the sum of the $\alpha$ decay into an excited state in $^{282}$Cn plus a few tens of keV attributed to atomic electron relaxation processes. Electron binding energies for the $K$ and $L$ shells in $Z = 112$ copernicium are $\approx 190$ keV and $\approx 40$ keV, respectively [51].

Based on the known average of $E_\alpha = 10.19(3)$ MeV extracted from in total fifteen of 29 hitherto observed decay chains [39], and thus $Q_\alpha = 10.33(3)$ MeV for the $^{286}$Fl ground-state to ground-state decay, two reasonable options for a decay scenario emerge for the $\alpha$-electron coincident event [39,41]. They are displayed in Fig. 4a,b, respectively. Using $Q_\alpha \approx 9.70 - 9.75$ MeV, $b_\alpha = 1/29$, and $T_{1/2} =$ 121 ms, a hindrance factor close to unity can be derived [39,52]. This clearly favours a $0^+$ spin-parity assignment to the excited state. In turn, this excited $0_2^+$ state can either directly decay into the ground-state via a $K$-converted $E0$ transition, or via an $E2$ cascade through the first excited $2_1^+$ state expected at $\approx 0.2$ MeV excitation energy. In that case, the observed electron stems from $L$ conversion, while the (converted) electromagnetic $2_1^+ \rightarrow 0_1^+$ decay escaped detection. For the first scenario, $E_\alpha = 9.60$ MeV ($Q_\alpha =$ 9.74 MeV), $E_e = 0.37$ MeV, and $E_{BE,K} = 0.19$ MeV sum to $E_{tot} = 10.16$ MeV ($Q_{tot} = 10.30$ MeV), which is within uncertainties in line with previously measured or averaged values. One can note that $E_\alpha = 10.16(1)$ MeV was measured with TASISpec for the second, full-energy $\alpha$-decay event of $^{286}$Fl [39]. For the scenario shown in Fig. 4b, $Q_\alpha = 9.71$ MeV, $E_e = 0.36$ MeV, $E_{BE,L} = 0.04$ MeV, $E(2^+) = 0.22$ MeV, plus some 30-40 keV atomic electron relaxation energy sum to $Q_{tot} = 10.33$ MeV, which is also within uncertainties in line with measured or average values.

Both decay scenarios were probed against Geant4 simulations, and both decay scenarios were assessed compatible with data, though finally with a slight preference for the scenario shown in Fig. 4a [21,41]. Nevertheless, and irre-

spective of the decay scenario, there is an excited $0^+$ state at $E_x \approx 0.6$ MeV in $^{282}$Cn, which requires a theoretical explanation. Based on contemporary beyond mean-field calculations exploring the full $\beta - \gamma$ deformation plane [9,10,53], shape coexistence is suggested and a pronounced magic shell gap at $Z = 114$ judged unlikely once again [39].

The global data set on $^{289}$Fl nuclei was roughly doubled, but for the first time the decay chains were interrogated with an $\alpha$-photon and $\alpha$-electron coincidence set-up [21,40]. Historically, after some early isotopic re-assignments, five decay chains starting from $^{289}$Fl were reported in experiments conducted at the Dubna Gas-Filled Recoil Separator (DGFRS) [43,45,54]. Four congruent decay chains were observed in TASCA experiments a few years later [42], including one recoil-$\alpha$–$\alpha$–$\alpha$ chain reaching $^{277}$Hs [47]. Indeed, this type of chain was confirmed twice in the TASISpec data [21,40]. Four additional $^{289}$Fl decay chains are part of the single-atom chemistry studies conducted behind TASCA [55,56], and nine indirect observations of $^{289}$Fl and its decay were documented following the $\alpha$ decay of $^{293}$Lv [46,48,49,54]. Based on rather broad $\alpha$-decay energy distributions of the existing measurements, which are displayed in Fig. 5a, b, and predicted single-particle states (cf. Fig. 6) one can anticipate both $\alpha$-decay fine structure and the potential for X-ray fingerprinting [12] along the decay chain of $^{289}$Fl.

The experimental energy spectra of the TASISpec measurement for the $\alpha$-decay steps $^{289}$Fl$\rightarrow^{285}$Cn and $^{285}$Cn$\rightarrow^{281}$Ds are displayed in Fig. 5c, d, respectively. Based on the rather large number of events for a single experiment, superior energy resolution, the observation of one $\alpha$-photon-

electron triple coincidence plus one $\alpha$-photon and $\alpha$-electron coincidence each, and following the self-consistency check with Geant4 simulations, the decay sequence sketched in Fig. 6a can be derived [21,40,41]: The main decay branch of $^{289}$Fl with $Q_\alpha = 9.94(2)$ MeV, which is indicated by blue arrows in Fig. 6a, proceeds (most likely) into a very low lying state at $\approx 30$ keV in $^{285}$Cn. Summing of the $\alpha$-decay energy and internal conversion electron energies explains the main peak in Fig. 5c, the FWHM of which is somewhat larger than expected for a single plain $\alpha$ decay like the one shown in Fig. 2b for even–even $^{288}$Fl. The triplet peak structure at some 9.1 MeV in Fig. 5d can only be explained by an $\alpha$ decay into an excited state at some 120-160 keV, which cascades to the ground state via a second, low lying excited state. All possible electromagnetic decays need to be dominated by internal conversion. A tentative third state in $^{281}$Ds at about 300 keV excitation energy relates to the 8.92(1)–0.25(1)-MeV $\alpha$-electron coincidence event, marked with a ★ in Fig. 5d. Depending on whether one puts more weight on the two photon energies [40] or the two conversion electron energies (manuscript VI in [21]) one ends up with numerically slightly different sequences of excitation energies (35–124–266 keV or 60–160–340 keV). However, and including the ground state in the count, the decisive message is the disclosure of a triplet (or quadruplet) of closely lying states of presumably the same parity and mutually connected by highly converted $M1$ and $E2$ transitions in $^{281}$Ds. The three decay chains reaching $^{277}$Hs have similar but not the same $\alpha$ energies measured [40,47]. This suggests a $Q_\alpha = 8.75(2)$-MeV decay into an excited state of $^{277}$Hs at $\approx 90$ keV, followed by a highly converted $M1$ transition into the ground state. A second, presumably independent $Q_\alpha = 9.70(3)$–9.17(6)-MeV sequence, indicated by the red arrows in Fig. 6a, can be distinguished from the main branch. Note, however, that implantation-decay time correlations are consistent with both branches starting from the same (ground) state of $^{289}$Fl: Combining all 25 known data points, $T_{1/2} = 2.3\binom{6}{4}$ s is obtained. Those 18 data points, which can be associated with the main branch, yield $T_{1/2} = 2.5\binom{8}{5}$ s, while the three data points for the low $\alpha$-energy branch imply $T_{1/2} = 2.9\binom{39}{10}$ s [21,40].

There are many examples available from many different types of nuclear structure models and parametrisations for ground-state to ground-state $Q_\alpha$ values, i.e., masses of super-heavy nuclei. At variance, published sequences of excited (single-particle) states and connecting $\alpha$-decay probabilities are surprisingly scarce in pertinent literature. Figure 6b–d show three available predictions for the $^{289}$Fl decay chain. Typical for odd-$N$ (odd-$Z$) nuclei in the superheavy regime is the competition between high-$\Omega$ Nilsson intruder orbitals from the spherical $\mathcal{N} = 7$, $j_{15/2}$ ($\mathcal{N} = 6$, $i_{13/2}$) shell and low-spin natural parity $\mathcal{N} = 6$ ($\mathcal{N} = 5$) states of opposite parity. An interesting side note is that occupancy or non-occupancy of these high-$\Omega$ intruders plays a central role in
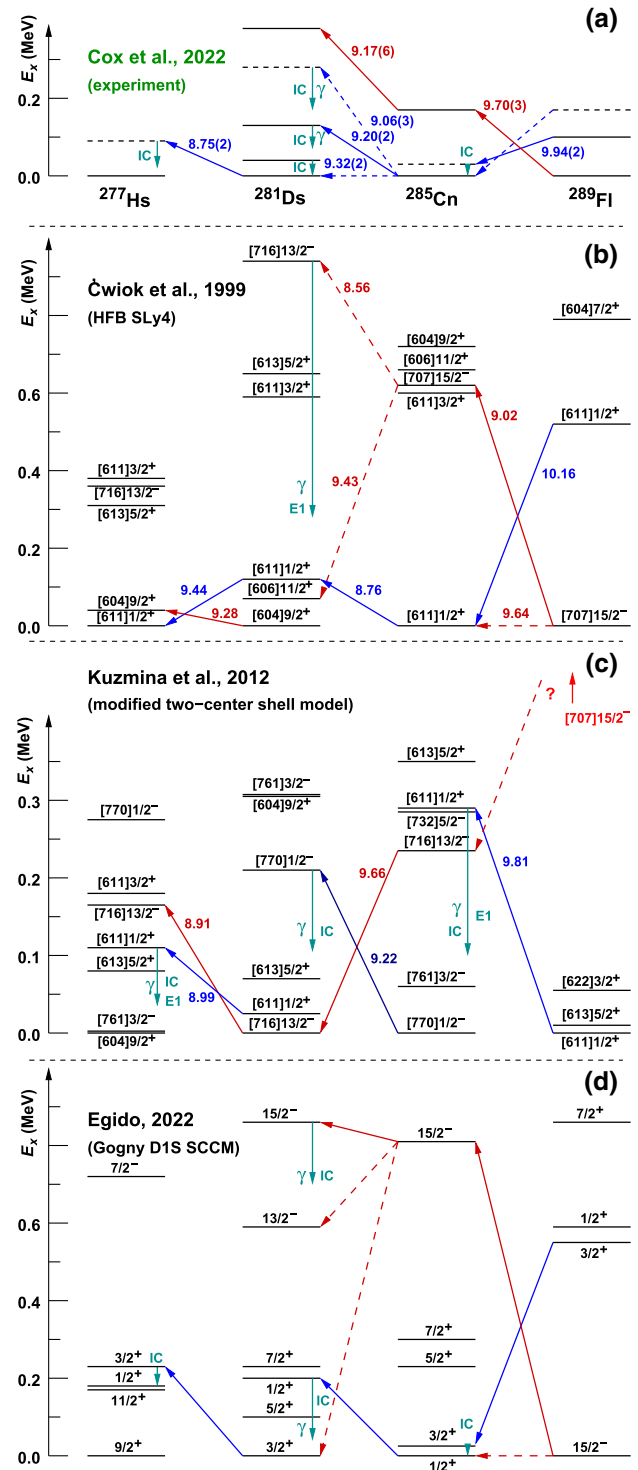


**Fig. 6 a** provides proposed experimental $\alpha$-decay chains of $^{289}$Fl [21,40]. The relative energy between the ground and first excited state in $^{289}$Fl is unknown (and can be zero). Dashed levels and $\alpha$-decay connections are tentative. See text and [21,40] for additional information. **b**–**d** are predicted single-particle energies along $^{289}$Fl decay chains and likely $\alpha$-decay transitions connecting high-$\Omega$ states (red) and low-$\Omega$ states (blue), respectively. Dashed lines are indicative for alternative branches. The decay schemes use numbers or are adopted from information provided by [57–59]. For the calculations shown in **a** and **b**, asymptotic Nilsson labels and calculated (ground-state to ground-state) $Q_\alpha$ values are available

"the interplay of single-particle shell structure, ground-state deformation and dynamic quadrupole collectivity" which can lead to deformation softness or shape coexistence [8]. For the $\alpha$-decay sequences of odd-$A$ superheavy nuclei, the competition between high-$\Omega$ and low-$\Omega$ levels implies a high probability for two (or more) $\alpha$-decay branches, because larger angular momentum difference between initial and final states must be compensated by a significant difference in decay energy to be competitive. In this respect, the superfluid tunneling model [60] is an interesting tool to investigate this kind of competitiveness, with excellent results on even–even [61] and odd-$A$ and odd-odd nuclei [62]. In view of the decay of $^{289}$Fl shown in Fig. 6b [57], for instance, the predicted 9.02-MeV $[707]15/2^- \rightarrow [707]15/2^-$ and 9.64-MeV $[707]15/2^- \rightarrow [611]1/2^+$ $\alpha$ transition probabilities become comparable in size, because $\Delta L = 7$ is found to be compensated by $\Delta Q \approx 0.5$ MeV in the framework of the superfluid tunneling model [62]. However, neither of the half-life predictions for these two branches, in fact a few hundred seconds, is compatible with the experimental observation. In turn, the 10.16-MeV decay from the excited $[611]1/2^+$ state in $^{289}$Fl results in a value close to experiment. However, two straight 8.76 and 9.44-MeV $[611]1/2^+ \rightarrow [611]1/2^+$ decays are expected to follow, which is at variance with the observed fine-structure in the decays into in particular $^{281}$Ds [cf. Fig. 5d] and $^{277}$Hs [cf. Fig. 6a]. In the model prediction shown in Fig. 6c, the $[611]1/2^+$ state is the predicted ground state, while the $\mathcal{N} = 7$ high-$\Omega$ levels are presumably beyond the applied 400-keV cut in excitation energy in the relevant Fig. 2 in [58]. These states do appear in the spectrum of the lighter nuclei though. The other difference is the appearance of low-lying negative-parity states, and the $\alpha$-decay pattern of that prediction is likely to follow a mix of low-spin positive and low-spin negative parity states. In principle, this can give rise to electromagnetic transitions, similar to experiment. Nevertheless, a $[611]1/2^+ \rightarrow [761]3/2^-$ transition requires a significant change in the underlying configurations. Hence, though $Q$-values are close to experiment and though there is energetically room for electromagnetic transitions, in particular the decay step $^{289}$Fl$\rightarrow^{285}$Cn is difficult to bring in accordance with experiment. There is no option for the separate low-$Q_\alpha$ sequence either. Finally, the predictions of the symmetry conserving configuration mixing, i.e., beyond mean-field calculations in the full $\beta - \gamma$ plane, provide an almost too good match with experiment following the anticipated decay path along positive-parity low-spin states [40,59]. Here, only the relatively large energy shift predicted for the $15/2^-$ intruder state is seemingly problematic. Interestingly, the very same model is also capable of explaining the smooth $Q_\alpha$ sequence across $^{288}$Fl and the low-lying state in $^{282}$Ds (see above and [39]).
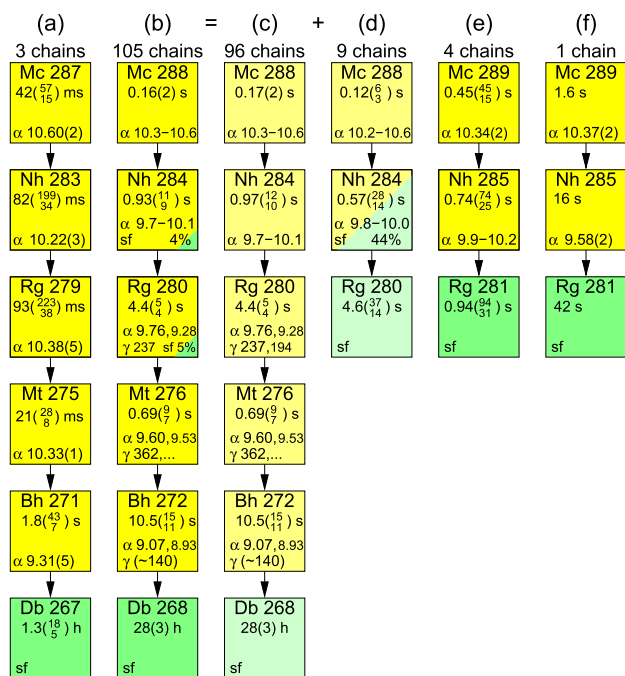
Clearly, the spectroscopy results obtained with TASISpec on the decay chain of $^{289}$Fl carry significant *direct* information to select between nuclear structure calculations of the heaviest elements.

## 4 Decay chains associated with Mc isotopes

The TASISpec 'element 115 experiment' was conducted in 2012. In total, 30 decay chains were associated with the isotopes $^{287}$Mc, $^{288}$Mc, and $^{289}$Mc [63,64]. Comprehensive information on the preparations and the experiment itself can be found in [20,22]. At about the same time, summarizing information on 37 decay chains observed in a series of experiments at Joint Institute for Nuclear Research (JINR) in Dubna and associated with isotopes of Mc was presented in [65], including the first four decay chains seen already in 2003 and published shortly after [66,67]. Undoubtedly, element 115 was discovered at Dubna. In 2015, another 46 $\alpha$-decay chains associated with $^{288,289}$Mc were reported as a result of a single experiment conducted at Lawrence Berkeley National Laboratory [68]. The latter experiment was, alike TASISpec, sensitive to $\alpha$-photon coincidences. All three data sets are based on the same fusion-evaporation reaction, namely $^{48}$Ca+$^{243}$Am, at by and large comparable beam energies at mid target.

The vast majority of the reported decay chains, 99 out of 113, comprise five $\alpha$-decay steps prior to concluding fission events. They are usually denoted 'long chains'. The remaining 'short chains' have either one (four chains) or two (ten chains) $\alpha$-decay steps detected prior to fission events. Three out of these 99 long chains are commonly assigned to start from $^{287}$Mc. This is based on various energy-energy, energy-time, and time-time correlations (cf. Fig. 2 in [69]), as well as the standard single-decay step 'Schmidt test' [70] (cf. Fig. 1 and Table 1 in [71]), and the more elaborate congruence check along $n$-step long decay chains [64,72]. The fact that the two $^{287}$Mc decay chains observed in Dubna experiments were produced at comparatively high beam energies supported their assignment to the $4n$-evaporation channel. The average values of the $^{287}$Mc chain are shown in Fig. 7a. Similarly, basic and advanced statistical methods probing the bulk of the long decay chains [69,71,72], while also applied to beam-energy dependent subsets, did *not* show any significant sign of *not* associating these 96 decay chains with the decay of one single radioactivity [64], i.e., starting from one (ground) state of odd–odd $^{288}$Mc. This isotope assignment was more recently confirmed by the first direct mass-number measurement of superheavy nuclei [73]. The average values of these 96 $^{288}$Mc chains are shown in Fig. 7c. Nevertheless, a note of caution might be appropriate here: Despite the majority of the data having been taken at beam energies near the anticipated peak cross section of the $3n$ evaporation channel, $^{288}$Mc, the ratio 3:96 of number of $^{287}$Mc:$^{288}$Mc chains is puzzling, given the rather broad excitation functions and

|  | (a) | (b) = | (c) + | (d) | (e) | (f) |
|---|---|---|---|---|---|---|
|  | 3 chains | 105 chains | 96 chains | 9 chains | 4 chains | 1 chain |
| Mc | Mc 287<br>42($^{57}_{15}$) ms<br>α 10.60(2) | Mc 288<br>0.16(2) s<br>α 10.3–10.6 | Mc 288<br>0.17(2) s<br>α 10.3–10.6 | Mc 288<br>0.12($^{6}_{3}$) s<br>α 10.2–10.6 | Mc 289<br>0.45($^{45}_{15}$) s<br>α 10.34(2) | Mc 289<br>1.6 s<br>α 10.37(2) |
| Nh | Nh 283<br>82($^{199}_{34}$) ms<br>α 10.22(3) | Nh 284<br>0.93($^{11}_{9}$) s<br>α 9.7–10.1<br>sf 4% | Nh 284<br>0.97($^{12}_{10}$) s<br>α 9.7–10.1 | Nh 284<br>0.57($^{28}_{14}$) s<br>α 9.8–10.0<br>sf 44% | Nh 285<br>0.74($^{74}_{25}$) s<br>α 9.9–10.2 | Nh 285<br>16 s<br>α 9.58(2) |
| Rg | Rg 279<br>93($^{223}_{38}$) ms<br>α 10.38(5) | Rg 280<br>4.4($^{5}_{4}$) s<br>α 9.76,9.28<br>γ 237 sf 5% | Rg 280<br>4.4($^{5}_{4}$) s<br>α 9.76,9.28<br>γ 237,194 | Rg 280<br>4.6($^{37}_{14}$) s<br>sf | Rg 281<br>0.94($^{94}_{31}$) s<br>sf | Rg 281<br>42 s<br>sf |
| Mt | Mt 275<br>21($^{28}_{8}$) ms<br>α 10.33(1) | Mt 276<br>0.69($^{9}_{7}$) s<br>α 9.60,9.53<br>γ 362,... | Mt 276<br>0.69($^{9}_{7}$) s<br>α 9.60,9.53<br>γ 362,... |  |  |  |
| Bh | Bh 271<br>1.8($^{43}_{7}$) s<br>α 9.31(5) | Bh 272<br>10.5($^{15}_{11}$) s<br>α 9.07,8.93<br>γ (~140) | Bh 272<br>10.5($^{15}_{11}$) s<br>α 9.07,8.93<br>γ (~140) |  |  |  |
| Db | Db 267<br>1.3($^{18}_{5}$) h<br>sf | Db 268<br>28(3) h<br>sf | Db 268<br>28(3) h<br>sf |  |  |  |

**Fig. 7** Overview of decay chains associated with $^{287}$Mc (**a**), $^{288}$Mc (**b**)–(**d**), and $^{289}$Mc (**e**)–(**f**). Panel **b** is the combination of the 96 long chains in **c** and the nine short chains in **d**. Panels **e** and **f** suggest two separate decay paths for odd-$A$ $^{289}$Mc, the latter representing the single statistical outlier 'D3'. Odd–odd isotopes with spontaneous fission (branches) in **b**–**d** may also undergo $\beta^+/EC$ prior to fast fission of their respective even–even daughters $^{284}$Cn, $^{280}$Ds, or $^{268}$Rf. See text for more discussion

near equal numbers of $3n$:$4n$ evaporation channels in case of Fl, $Z = 114$, and Lv, $Z = 116$ isotopes. A possible explanation is that another type of $^{287}$Mc chain (see below) has decay characteristics, which so far are statistically indistinguishable from those associated with $^{288}$Mc.

From a nuclear structure point of view, the observation [63] and confirmation [68] of a 237-keV $E1$ $\gamma$ ray in $^{276}$Mt provides an intriguing benchmark for nuclear structure theory. It relates to the relative positioning of high-$\Omega$ intruder orbitals vs. low-$\Omega$ natural orbitals already discussed in connection with the observed fine structure along $^{289}$Fl decay chains. Depending on deformation and nuclear structure model, it turns out that there are essentially only two options for $E1$ emission in $^{276}$Mt (at $\beta_2 \approx 0.2$): a $\pi[615]11/2^+ \rightarrow \pi[505]9/2^-$ or a $\nu[716]13/2^- \rightarrow \nu[606]11/2^+$ transition. Accordingly, at least one of these combinations of Nilsson orbitals must be close to the Fermi surface in $^{276}$Mt. This has been nicely illustrated with calculations using contemporary Skyrme energy density functionals [74]. The parameter set UNEDF1$^{SO}$, which was optimized for heavy $Z \approx 100$, $A \approx 250$ nuclei, fails to place any of the two combinations at the Fermi surface for $^{276}$Mt. In turn, the standard UNEDF1 parameter set does suggest the $E1$ in the proton sector. This

is discussed in detail in [74] and highlighted in connection with Fig. 2 in [38].

Supported by dedicated Geant4 simulations [31–33], it is possible to probe, study, and suggest various decay schemes along the $^{288}$Mc chain. For the first two steps, $^{288}$Mc$\rightarrow^{284}$Nh and $^{284}$Mc$\rightarrow^{280}$Rg, hardly any $\alpha$-photon coincidence was observed [63,68]. However, rather broad decay-energy distributions were measured consistently in all three data sets [63,65,68]. From these investigations, (ground-state to ground-state) $Q_\alpha$ values of 10.7(1) and 10.2(1) MeV, respectively, could be extracted [71,75]. For $^{280}$Rg$\rightarrow^{276}$Mt, $Q_\alpha = 10.15(1)$ MeV follows from the coincidence of $E_\alpha = 9.76(1)$-MeV $\alpha$ particles with 237-keV $\gamma$ rays [63,68]. Similarly, with $E_\alpha = 9.60(1)$-MeV $\alpha$ particles being coincident with 362-keV $\gamma$ rays [63,68], $Q_\alpha = 10.10(1)$ MeV follows for the decay of $^{276}$Mt. For the last decay step, $^{272}$Bh$\rightarrow^{268}$Db, $Q_\alpha = 9.21(1)$ MeV follows directly from a prominent $E_\alpha = 9.07(1)$-MeV $\alpha$-decay branch. It is worth noting that the beginning of the $Q_\alpha$-series, i.e., when decay chains starting from Mc chains cross $Z = 114$, cannot be reproduced by models relying on a pronounced shell gap at just $Z = 114$ (cf. Fig. 4 in [75]).

$K$ X-ray candidates at proper photon energies are present in spectra coincident with the $^{280}$Rg [68,71] and $^{276}$Mt $\alpha$ decays [63,68,71]. However, unequivocal fingerprinting of the proton number like, for instance, for rutherfordium [12] is not possible with the at present still limited number of $\alpha$-photon coincidence events. The reasons are either the seemingly complex $\gamma$ decay scheme of $^{272}$Bh [63,68,76], or the relatively small conversion coefficients of the $E1$ transitions in $^{276}$Mt [63,68]. In either case, they can lead to background at the $K$ X-ray energies of interest due to Compton scattered events [71].

For consistency, the fourteen short recoil-$\alpha$(-$\alpha$)-fission chains are labelled according to [64,72,77], i.e., D1–D4 for four such chains reported from Dubna [65], T1–T7 for the seven chains detected with TASISpec [64], and B1–B3 for the three chains observed in the Berkeley experiment [68]. Based on standard statistical assessments of correlation times per single decay step [69,70,77] and more elaborate tests of correlation times along decay chains [20,64,72,77], it has been shown that the hypothesis of this set of fourteen decay chains forming a single congruent ensemble can be falsified with an error probability of $< 1\%$. The straight-forward solution is to single out decay chain D3 and associate it with the $2n$ evaporation channel $^{289}$Mc, as it is done in Fig. 7f. This action is further supported by the reported $\alpha$-decay energies of D3; for the first decay step, it is lower than the vast majority of decay chains associated with $^{287,288,289}$Mc, and it lies clearly outside the common range of energies for the second decay step (see, for instance, Fig. 1 in [64], Fig. 1 in [77], or Fig. 2 in [69]).

The correlation times of the remaining thirteen short chains were found to be compatible with representing one ensemble [64,72,77], and two extreme but in terms of correlation-time analyses sound cases have been studied and presented in depth in [64]: All thirteen chains either form a separate, second $^{289}$Mc decay chain, or all thirteen chains could be readily combined with the long decay chain of $^{288}$Mc. This leads to either small fission or $\beta^+$/EC branches of $^{284}$Nh and $^{280}$Rg, in the latter case followed by fast fission of the even-even daughters $^{284}$Cn or $^{280}$Ds (cf. Sect. 3). Further alternatives for distributing the short chains amongst Mc isotopes have already been suggested (see, for instance, [64] p. 132). Here, one fraction of nine short chains is combined with the 96 long $^{288}$Mc chains, based on favourable congruence tests with that well-established ensemble *and* $E_\alpha$(Mc) > 10.4 MeV. This set is shown in Fig. 7d. Together with the 96 long chains, it gives rise to a statistically and energetically sound ensemble of 105 decay chains starting from $^{288}$Mc. It is illustrated in Fig. 7b. The remaining four short chains (D1, D4, T4, T7) – with less favourable congruence test results and $E_\alpha$(Mc) < 10.4 MeV – are *suggested* to form the second decay path of $^{289}$Mc illustrated in Fig. 7e. Three comments: First, in terms of the statistical assessments of the correlation times, this two-split into nine short $^{288}$Mc and four short $^{289}$Mc chains remains arbitrary. In fact, B3 and D4 may fit $^{287}$Mc best [64], and either one may be the result of a $2n$ reaction on a small $^{241}$Am fraction of the enriched $^{243}$Am target material. Second, the decay-energy cut at 10.4 MeV relates to the fact that all decay chains starting from element 117, tennessine, report $E_\alpha$(Mc) < 10.4 MeV (see Sect. 5). Third, there could be even more decay paths and connections [62].

The nuclear structure aspects of having two similar but different decay paths of $^{289}$Mc have been discussed previously (see Fig. 3 in [64]). In accordance with the discussions of fine-structure pathways of $^{289}$Fl (cf. Fig. 6) and $^{293}$Ts (cf. Fig. 11), high-$\Omega$ $\mathcal{N}=6$ [606]13/2$^+$ or [615]11/2$^+$ positive-parity Nilsson orbitals are predicted to form one decay path, and low-$\Omega$ $\mathcal{N}=5$ negative-parity orbitals are suggested to form the other one. Other models predict [78], or at least indicate [79], the same pattern of at least two possible decay paths of $^{289}$Mc, while details like $Q_\alpha$ values, half lives, hindrance factors, or overall complexity are model dependent and eventually require detailed assessments of $\alpha$-decay probabilities [62].

As expected, predictions are comparable for $^{287}$Mc, but with less evidence for two parallel decay paths for some of them. Figure 8 shows the few available examples, representing in panel Fig. 8a a macroscopic-microscopic approach based on the Woods-Saxon potential [80], in panel Fig. 8b a modified two-center shell-model approach adopted from Fig. 1 of [78], and in panel Fig. 8c the Skyrme energy-density functional UNEDF1 using numbers from Tables IV–VI of
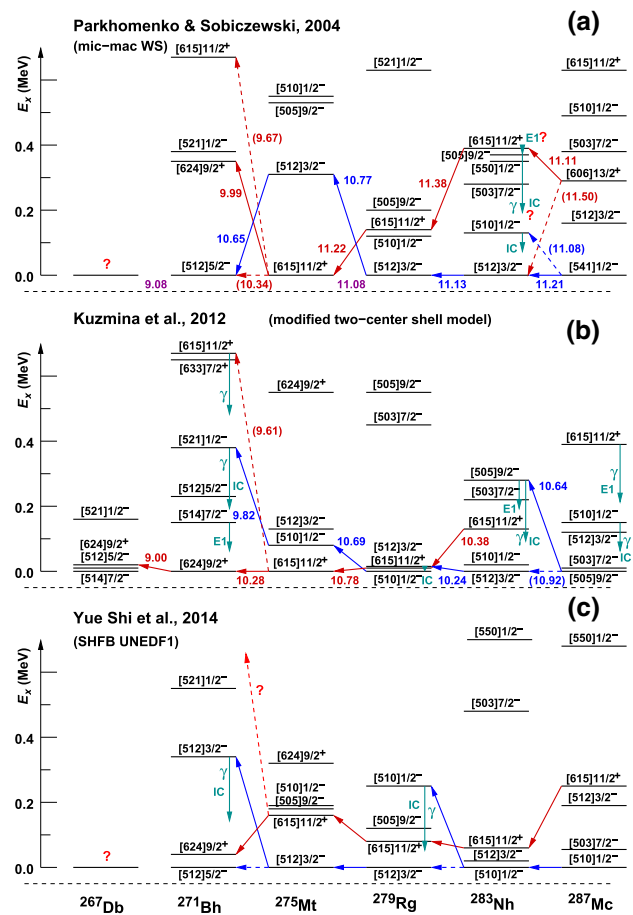


**Fig. 8** Predicted single-particle energies along $^{287}$Mc decay chains and likely $\alpha$-decay transitions connecting high-$\Omega$ positive-parity states (red) and negative-parity states (blue), respectively. Dashed lines are indicative of alternative branches. The decay schemes use numbers or are extracted from information provided by [74,78,80]. Asymptotic Nilsson labels are used, and calculated (ground-state to ground-state) $Q_\alpha$ values are included provided availability [78,81]

[74]. In comparison, the experimental $Q_\alpha$ values of the $^{287}$Mc decay chain are 10.75(2), 10.37(3), 10.53(5), 10.48(1), and 9.45(5) MeV [cf. Fig. 7a]. These are consistently higher than those derived for the $^{288}$Mc chain [$Q_\alpha = 10.7(1)$, 10.2(1), 10.15(1), 10.10(1), and 9.21(1) MeV], a given fraction of which might form the anticipated second decay path of $^{287}$Mc (see above).

The macroscopic–microscopic model predicts at least two different $\alpha$ decays starting from either the [606]13/2$^+$ level at $E_x = 0.29$ MeV or the [541]1/2$^-$ ground state of $^{287}$Mc. The latter populates low-spin negative-parity states in the daughter $^{283}$Nh, and its [512]3/2$^-$ ground state is predicted to continue to $\alpha$ decay into ground or excited states of the same or similar Nilsson orbitals. On average, the predicted $Q_\alpha$ values [81] are close to experiment, including the drop in the last decay step. Note that Nilsson single-particle states in $^{267}$Db are lacking in [80]. There is a risk

**Table 1** Overview of correlation-time analyses of single decay steps according to [70] of the first four decay steps of the long tennessine chains previously assigned to start from $^{294}$Ts (L294). The ensemble S293A is taken from the second column of Table 2 for completeness. The combination with the moscovium chain D3, which is also singled out in Fig. 7f, is presented in the rightmost column. The tag 'H' indi-cates a failed 'Schmidt test'. The labels of the ensembles are defined in the text and Fig. 9. The energy intervals comprise 90% of the yield of the Gaussian-weighted sum spectra, unless there are peaks noticeable. Decay data of individual chains starting from element 117, tennessine, are taken from [77,85,87]

| Label | S293A | L294 | M29X | D3 | L29X |
|---|---|---|---|---|---|
| No. of chains | 7 | 6 | 13 | | 13+1 |
| $T_{1/2}(Z=117)$ (ms) | $42\binom{29}{12}$ | $54\binom{43}{17}$ | $46\binom{20}{11}$ | n/a | see M29X |
| data points; $\sigma_{\Theta_{exp}}$ | 6 ; 0.99 | 5 ; 1.26 | 11 ; 1.12 | | |
| $[\sigma_{\Theta,low}, \sigma_{\Theta,high}]$ | [0.48, 1.89] | [0.41, 1.90] | [0.67, 1.81] | | |
| data points; $E_{decay}$ (MeV) | 5+1 ; [10.87, 11.13] | 5 ; [10.76, 11.11] | 10+1 ; [10.80, 11.11] | | |
| | 10.60(2) | | 10.60(2) | | |
| $T_{1/2}(Z=115)$ (s) | $0.44\binom{44}{15}$ | $0.65\binom{52}{20}$ | $0.55\binom{28}{14}$ | 1.6 | $0.66\binom{31}{16}$ |
| data points; $\sigma_{\Theta_{exp}}$ | 4 ; 0.80 | 5 ; 1.61 | 9 ; 1.31 | | 10 ; 1.35 |
| $[\sigma_{\Theta,low}, \sigma_{\Theta,high}]$ | [0.31, 1.92] | [0.41, 1.90] | [0.62, 1.84] | | [0.65, 1.82] |
| data points; $E_{decay}$ (MeV) | 5 ; 10.22(3) | 6 ; 9.78(3), 10.27(3) | 11 ; [10.12, 10.36] | 10.37(2) | 12 ; [10.12, 10.40] |
| $T_{1/2}(Z=113)$ (s) | $4.7\binom{38}{14}$ | $9.6\binom{66}{28}$ | $7.3\binom{32}{17}$ | 16 | $8.0\binom{33}{18}$ |
| data points; $\sigma_{\Theta_{exp}}$ | 5 ; 1.88 | 6 ; 1.02 | 11 ; 1.65 | | 12 ; 1.65 |
| $[\sigma_{\Theta,low}, \sigma_{\Theta,high}]$ | [0.41, 1.90] | [0.48, 1.89] | [0.67, 1.81] | | [0.70, 1.79] |
| data points; $E_{decay}$ (MeV) | 7 ; 9.47(3), 9.71(4) | 5 ; [9.53, 9.82] | 12 ; [9.41, 9.85] | 9.58(2) | 13 ; [9.41, 9.85] |
| $T_{1/2}$ (Rg) (s) | $32\binom{19}{9}$ | $103\binom{71}{30}$ | $64\binom{25}{14}$ | 42 | $62\binom{23}{13}$ |
| data points; $\sigma_{\Theta_{exp}}$ | 7 ; 1.29 | 6 ; 2.09 H | 13 ; 1.74 | | 14 ; 1.68 |
| $[\sigma_{\Theta,low}, \sigma_{\Theta,high}]$ | [0.52, 1.87] | [0.48, 1.89] | [0.72, 1.77] | | [0.73, 1.77] |
| data points; $E_{decay}$ (MeV) | SF | 5 ; 8.86(3), 9.02(3) | see L294 | SF | see L294 |

that the high-$\Omega$ chain merges into the low-$\Omega$ chain already in $^{285}$Nh. The [606]13/2$^+$ level decays most likely into the [615]11/2$^+$ state, which does involve some hindrance. Since the [505]9/2$^-$ level is predicted 20 keV below this [615]11/2$^+$ level, there is a chance for a very low-energy $E1$ decay, which leads to an electromagnetic decay cascade down to the ground state of $^{283}$Nh. There is also a chance for a competing direct $\alpha$ decay of the [606]13/2$^+$ state into the [512]3/2$^-$ ground state of $^{283}$Nh, because the extra $\approx 0.4$ MeV in $Q_\alpha$ may account for $\Delta L = 5$ [62]. If the $E1$ decay of the [615]11/2$^+$ is not possible, a separate high-$\Omega$ sequence can evolve. However, its $Q_\alpha$ pattern is at variance with the values measured for $^{287,288}$Mc.

For the modified two-center shell-model approach [78], there is only one $\alpha$-decaying level predicted, namely the [505]9/2$^-$ ground state of $^{287}$Mc. Interestingly, the corresponding Nilsson state in the daughter lies at $E_x = 0.28$ MeV excitation energy, and clearly above the [615]11/2$^+$ level, with a favourable $E1$ in between. There is thus the option of entering the positive-parity high-$\Omega$ $\alpha$-decay sequence in $^{283}$Nh. The $Q_\alpha$ values, 10.64, 10.38, 10.78, 10.28, and 9.00 MeV, are matching the experimental ones rather well. Alternatively, the separate low-$\Omega$ chain may be entered via both an electromagnetic decay cascade of the excited [505]9/2$^-$ state in $^{283}$Nh, or a direct ground-state to

ground-state $\alpha$ decay, because $\Delta Q_\alpha = 0.28$ MeV may compensate hindrance due to the change in angular momentum.

The Skyrme energy density functional approach [74] suggests two separate decay sequences from start to end with similar $Q_\alpha$ values; the high-$\Omega$ chain proceeds mainly via the [615]11/2$^+$ level, but eventually switches to [624]9/2$^+$ in $^{271}$Bh. The low-$\Omega$ chain follows the [510]1/2$^-$ ground states in Mc and Nh, before it either directly or via electromagnetic decay reaches the [512]3/2$^-$ ground state of $^{279}$Rg. A similar pattern is predicted to occur for the $\alpha$ decay from $^{275}$Mt into $^{271}$Bh. Notably, in theory at least, these two $M1$ decays, let it be $E_\gamma \approx 0.25$ MeV [510]1/2$^-$ $\to$ [512]3/2$^-$ in $^{279}$Rg or $E_\gamma \approx 0.34$ MeV [512]3/2$^-$ $\to$ [512]5/2$^-$ in $^{271}$Bh, form perfect X-ray fingerprinting cases. Predictions for $^{267}$Db are not part of [74], and $Q_\alpha$ values are not given there either.

## 5 How to connect moscovium and tennessine?

Hitherto, in total 24 decay chains originating from isotopes of element 117, tennessine, have been reported [82–87]. The first decay chains were observed at Dubna via the reaction $^{48}$Ca+$^{249}$Bk [82,83]. The enriched $^{249}$Bk target material was provided by Oak Ridge National Laboratory. Given the rather short half life of $T_{1/2} = 330(4)$ y, the production, extraction,

**Fig. 9** Overview of decay chains associated with isotopes of tennessine. Panel **c** shows the average values for six long chains, L294, panel **d** for seven out of 18 reported short chains, S293A. Panel **b** combines these two sets into M29X, and panel **a** includes also chain D3 displayed in Fig. 7f. Panel **e** shows average values for the remaining eleven short chains, S293B, which is combined with the four moscovium chains shown in Fig. 7e. See text for more discussion

and isotopic enrichment of the required amount of tens of milligrams is a major effort [88,89], awarded with the name of the element a few years later [90,91].

In connection with a second round of provision of $^{249}$Bk material from Oak Ridge, experiments at Dubna and GSI confirmed the early findings [84–87]. Similar to the decay chains starting from moscovium isotopes (cf. Fig. 7), 'long' and 'short' decay chains from tennessine have been observed. The six long chains, four from Dubna experiments [85], two from the GSI experiment [86], comprise up to seven $\alpha$ decays. Their correlation times are statistically sound [72] and the $\alpha$-decay sequence is commonly assigned to the odd–odd isotope $^{294}$Ts. This ensemble of six chains is labelled 'L294' in the following. It is summarized in Table 1, and it is illustrated in Fig. 9c.

The situation is more complicated for the by now in total eighteen reported short decay chains. Sixteen were observed

in Dubna [85] but only two at GSI [87]. All of them have been assigned to start from the isotope $^{293}$Ts. They comprise either three $\alpha$-decay steps, i.e., conclude with a spontaneous fission of $^{281}$Rg, or four $\alpha$-decay steps, i.e., conclude with a spontaneous fission of $^{277}$Mt. The former refer to fourteen Dubna chains, while the latter relate to two chains from Dubna and both chains from GSI.

Decay chains populated via $^{249}$Bk($^{48}$Ca,4$n$)$^{293}$Ts feed those populated via $^{243}$Am($^{48}$Ca,2$n$)$^{289}$Mc. This kind of cross bombardment provides one out of several means [92] for isotope assignments and element discovery stories [93,94]. In fact, the official approval case of discovery of element 115 and element 117, published early 2016, relies primarily if not exclusively on the above mentioned cross bombardment. Unfortunately, the case is built upon the four in themselves non-congruent [72,77] short moscovium decay chains reported from Dubna [65], in combination with a subset of ten out of the sixteen short tennessine decay chains reported from Dubna [85]. Notably, neither these ten nor all sixteen or eighteen short tennessine decay chains are compatible with a single radioactivity either [72,77]. For instance, already the first decay step does not pass the 'Schmidt test', as shown in Table for the corresponding ensemble labelled 'S293'. In essence, the two elements were approved based on a hypothesis[1] which can be *falsified* on the 2-$\sigma$ level [72,77]. Moreover, the approval case also ignored the short moscovium chains detected at GSI and Berkeley, which were (made) available prior to approval [68,95], and which clearly show that the Dubna chain D3 is an outlier [77] [cf. Sect. 3 and Fig. 7f]. In fact, the task is to investigate ensemble S293 in more detail to identify a spot for the peculiar moscovium decay chain D3, and as a result *suggest* an alternative but statistically sound connection of decay chains of the two elements based on current world data.

There are many correlations between decay energies and correlation times between the first few decay steps of tennessine chains that can be studied. A selection of four correlations is displayed in Fig. 10. Based on such correlations and subsequently probing any single of the short tennessine chains against a reference chain formed by the congruent long tennessine chains, in the same fashion as it had been done

---

[1] It is important to state that the discussion in this contribution does not intend to challenge the discovery, naming rights, or the element names of moscovium and tennessine. There is clear evidence and there are many good arguments that isotopes of these two elements were discovered in joint Russian-US experiments conducted at JINR Dubna. In fact, a statistically sound cross-bombardment link between the two elements is suggested here. Further, congruent long decay chains reported first from Dubna have been confirmed in several independent experiments at GSI and Berkeley. The point is that many aspects of the report forming the basis of official approval are scientifically questionable. That report is a good case for a university course in science ethics – go ahead and identify mathematical and methodological flaws and debatable use of previously published material.
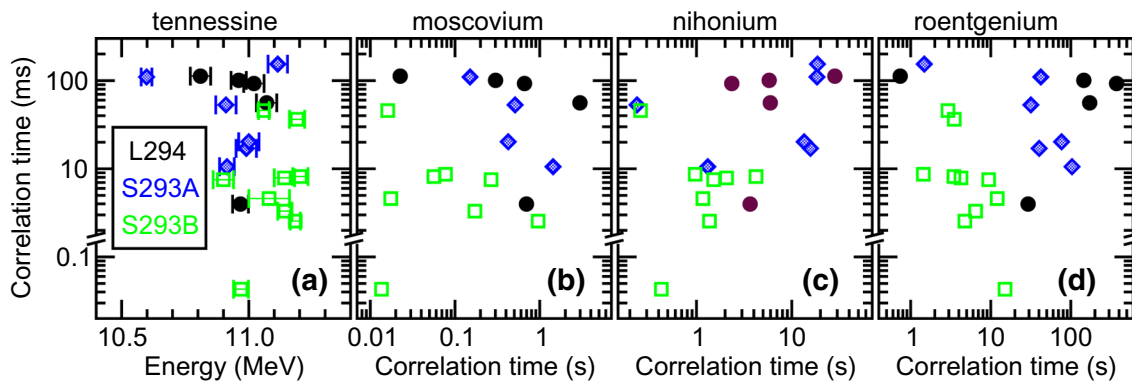
**Fig. 10** Correlations for ensembles L294 (black filled circles, cf. Table 1), S293A (blue shaded diamonds, cf. Tables 1 and 2), and S293B (green open squares, cf. Table 2). Correlation times reported for recoil-$\alpha$ events of isotopes of tennessine are plotted on the $y$ axis, while the $x$ axes refer to their decay energies (**a**) as well as the correlation times between Ts-Mc events (**b**), Ts-Nh events (**c**), and Ts–Rg events (**d**). In case of missing $\alpha$ events along the chain, subsequent correlation times were corrected for the half life of the missing decay step. This has not been done for the numerical analysis in the two tables

**Table 2** Same as Table 1 but for decay steps of short decay chains of tennessine, namely $^{293}$Ts. In the rightmost columns the combination with four short decay chains of moscovium (S289) is assessed. The latter are summarized in Fig. 7e and described in Sect. 4. The ensembles S293A, S293B, and S293C are illustrated in Fig. 9d–f. Decay data of individual chains starting from element 117, tennessine, are taken from [77,85,87]

| Label | S293 | S293A | S293B | S289 | S293C |
|---|---|---|---|---|---|
| No. of chains | 18 | 7 | 11 | 4 | S293B+S289 |
| $T_{1/2}(Z=117)$ (ms) | $21\binom{7}{4}$ | $42\binom{29}{12}$ | $8.7\binom{40}{21}$ | n/a | see S293B |
| data points; $\sigma_{\Theta_{exp}}$ | 16 ; 1.84 H | 6 ; 0.99 | 10 ; 1.82 | | |
| $[\sigma_{\Theta,low}, \sigma_{\Theta,high}]$ | [0.77, 1.75] | [0.48, 1.89] | [0.65, 1.82] | | |
| data points; $E_{decay}$ (MeV) | 14+2; [10.89, 11.21] | 5+1 ; [10.87, 11.13] | 9+1 ; [10.90, 11.22] | | |
| | 9.70(8), 10.60(2) | 10.60(2) | 9.70(8) | | |
| $T_{1/2}(Z=115)$ (s) | $0.24\binom{10}{5}$ | $0.44\binom{44}{15}$ | $0.14\binom{7}{4}$ | $0.45\binom{45}{15}$ | $0.24\binom{10}{5}$ |
| data points; $\sigma_{\Theta_{exp}}$ | 12 ; 1.53 | 4 ; 0.80 | 8 ; 1.43 | 4 ; 1.26 | 12 ; 1.57 |
| $[\sigma_{\Theta,low}, \sigma_{\Theta,high}]$ | [0.70, 1.79] | [0.31, 1.92] | [0.58, 1.85] | [0.31, 1.92] | [0.70, 1.79] |
| data points; $E_{decay}$ (MeV) | 13 ; [10.09, 10.42] | 5 ; 10.22(3) | 8 ; 10.33(2) | 3; 10.34(2) | 11 ; 10.34(2) |
| $T_{1/2}(Z=113)$ (s) | $2.5\binom{10}{6}$ | $4.7\binom{38}{14}$ | $0.98\binom{60}{27}$ | $0.74\binom{74}{25}$ | $0.89\binom{39}{21}$ |
| data points; $\sigma_{\Theta_{exp}}$ | 12 ; 1.40 | 5 ; 1.88 | 7 ; 0.84 | 4 ; 1.74 | 11 ; 1.30 |
| $[\sigma_{\Theta,low}, \sigma_{\Theta,high}]$ | [0.70, 1.79] | [0.41, 1.90] | [0.52, 1.87] | [0.31, 1.92] | [0.67, 1.81] |
| data points; $E_{decay}$ (MeV) | 13+2 ;[9.56, 9.96] | 7 ; 9.47(3), 9.71(4) | 8 ; 9.85(3) | 3 ; 9.89(1) | 11 ; 9.86(2) |
| | 9.47(3) | | | 10.18(2) | 10.18(2) |
| $T_{1/2}$ (Rg) (s) | $16\binom{5}{3}$ | $32\binom{19}{9}$ | $4.3\binom{22}{31}$ | $0.94\binom{94}{31}$ | $3.6\binom{16}{8}$ |
| data points; $\sigma_{\Theta_{exp}}$ | 16 ; 1.34 | 7 ; 1.29 | 9 ; 0.73 | 4; 1.37 | 11 ; 1.42 |
| $[\sigma_{\Theta,low}, \sigma_{\Theta,high}]$ | [0.77, 1.75] | [0.52, 1.87] | [0.62, 1.84] | [0.31, 1.92] | [0.67, 1.81] |
| data points; $E_{decay}$ (MeV) | 4 ; 9.31(5) | SF | 4 ; 9.31(5) | SF | 4 ; 9.31(5) |
| $T_{1/2}$ (Mt) (ms) | $4\binom{4}{1}$ | n/a | see S293 | | see S293 |
| data points; $\sigma_{\Theta_{exp}}$ | 4 ; 1.92 | | | | |
| $[\sigma_{\Theta,low}, \sigma_{\Theta,high}]$ | [0.31, 1.92] | | | | |
| data points; $E_{decay}$ (MeV) | SF | | | | |

for moscovium chains [64], it is suggestive to split ensemble S293 into S293A (seven chains) and S293B (eleven chains). Details are provided in Table 2, while S293A is also listed in Table 1 for completeness. In the notation of [77], ensemble S293A consists of S01, S04, S05, S08, S09, S10, and S15.

Figure 10a shows that on average somewhat higher decay energies correlate with somewhat smaller correlation times, and that the entries of ensemble S293A (blue) are similar to those of ensemble L294 (black). The difference between S293A and S293B (green) becomes more pronounced when looking at the time-time correlations in panels b–d: Data points in green tend to be located in the lower left triangle, all the others towards the upper right section in each of the three plots. In the advanced statistical test, chains S01, S04, S05, S09, and S10 show values similar to the long chains themselves, while the overlap is somewhat weaker for S08. S15 (missing first $\alpha$ decay) is a rather arbitrary choice based on its reported decay energies. If one compares column S293A in Table 1 with the reference column L294, they obviously fit well together both in terms of derived half lives and decay-energy ranges, i.e., they can very well be considered forming the same decay chain with an $\approx 50\%$ fission branch at roentgenium. This option is illustrated in Fig. 9b–d. Moreover, this mixed ensemble M29X provides an excellent explanation for decay chain D3 associated with $^{289}$Mc. This can also be seen in the respective columns of Table 1. Here, all five D3 observables, i.e., three correlation times and two decay energies, are found compatible with ensemble M29X. The final suggestion for these $6 + 7 + 1 = 14$ chains is displayed in Fig. 9a. For chain D3, either representing the $1n$-channel of the reaction $^{48}$Ca+$^{243}$Am or being due to a reaction on $^{244}$Am target nuclei is unrealistic. Therefore, the combined ensemble L29X forms a decay sequence of $^{293}$Ts rather than $^{294}$Ts. A possible counter argument arises from the reported mid-target beam energies and thus initial $^{297}$Ts$^{\star}$ compound nucleus excitation energies. However, and folding in GSI data on element 117, the combined cross-section plot shown as Fig. 8 in [87] turns out to be ambiguous. One may recall that setting up the planned beam energy and then maintaining it over long periods and presumably different beam tunes can be a challenging task at cyclotron facilities.

The remaining eleven short tennessine decay chains, S293B in Table 2 and Fig. 9e, form a consistent ensemble in themselves, i.e., there is no need for an additional split. In Table 2 and Fig. 9f they are combined with four chains associated with $^{289}$Mc, the latter based on $E_\alpha$(Mc)< 10.4 MeV, as mentioned earlier. These four chains end in $^{281}$Rg, like seven out of the eleven chains of the S293B ensemble. It may therefore be tempting to separate those four S293B chains ending in $^{277}$Mt. However, statistically it is not a major problem that four out of eleven tennessine decay chains yield an $\alpha$-decay branch of $^{281}$Rg, but none of the four moscovium chains. With the alternative association of chain
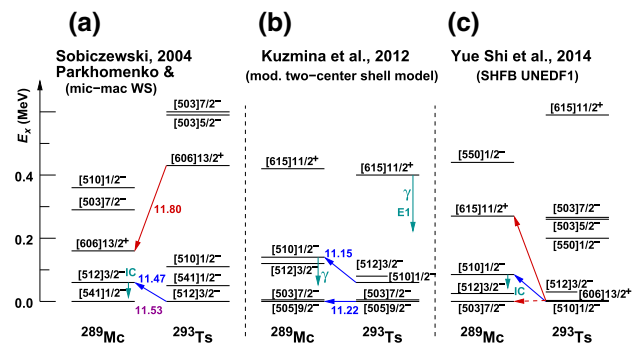


**Fig. 11** Predicted single-particle energies for $^{293}$Ts and $^{289}$Mc and likely $\alpha$-decay transitions connecting high-$\Omega$ positive-parity states (red) and negative-parity states (blue), respectively. The decay schemes use numbers or are adopted from information provided by [74,78,80]. Asymptotic Nilsson labels are used, and calculated (ground-state to ground-state) $Q_\alpha$ values are included provided availability [78,98]

D4 with $^{241}$Am($^{48}$Ca,2$n$)$^{287}$Mc or $^{243}$Am($^{48}$Ca,4$n$)$^{287}$Mc (cf. $E_\alpha$(Nh)> 10.1 MeV) the statement would read: none out of three. In any case, the combination of ensemble S293B with S289 provides another possible link between decay chains starting from isotopes of tennessine and moscovium, respectively. Two additional notes might be in place. First, concerning Fig. 9f, (partial) fission half lives of $^{281}$Rg ($T_{1/2,\mathrm{SF}} = 4.9(^{21}_{11})$ s) and $^{277}$Mt ($T_{1/2,\mathrm{SF}} = 4(^{4}_{1})$ ms) are close to those of the neighbouring even-$Z$ odd-$N$ nuclei $^{281}$Ds ($T_{1/2,\mathrm{SF}} = 21(^{4}_{3})$ s) and $^{277}$Hs ($T_{1/2,\mathrm{SF}} = 18(^{25}_{7})$ ms), respectively. Second, the half lives derived for ensemble S293B are in close to perfect agreement with those of the 105 decay chains associated with $^{288}$Mc. At variance, decay energies and fission branches at $Z = 111$ are not. Nevertheless, this shows that in particular the hitherto analysed $\alpha$-decay steps of Mc and Nh isotopes are very similar and thus difficult to disentangle. Therefore, in conclusion, the combined decay chains of tennessine and moscovium shown in Fig. 9a, f and listed in the rightmost columns of Tables 1 and 2 , respectively, both starting with $^{293}$Ts, are one possible solution of the task outlined earlier, but neither an exclusive one, nor is the final word claimed to be spoken.

Under the assumption that there are two parallel decay chains starting from $^{293}$Ts, they can be confronted with the few available calculations of single-particle Nilsson states of $^{293}$Ts and its $\alpha$-decay daughter $^{289}$Mc. The predictions of three models are illustrated in Fig. 11. The microscopic-macroscopic approach of Parkhomenko and Sobiczewski [80] suggests two parallel $\alpha$-decay sequences, but with somewhat too high $Q_\alpha$ values compared with $Q_{\alpha,\mathrm{exp}} \approx 11.2 - -11.3$ MeV: The decays are expected to proceed between the [606]13/2$^+$ high-$\Omega$ and [512]3/2$^-$ low-$\Omega$ orbitals, respectively. The two-center shell-model approach by Kuzmina et al. [78] predicts a [505]9/2$^-$ ground state followed by an almost degenerate [505]7/2$^-$ excited state, similar to
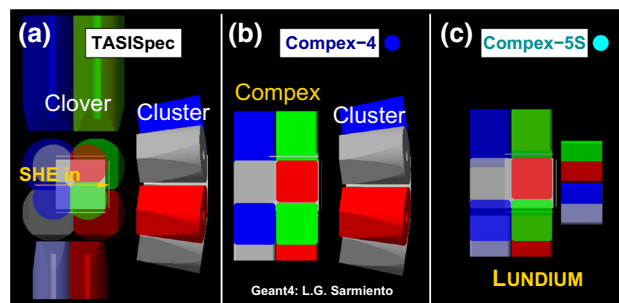
$^{289}$Mc and $^{287}$Mc [cf. Fig. 8b]. This implies that excited high-$\Omega$ positive-parity states can decay by $\gamma$-ray emission into the [505]9/2$^-$ ground state of $^{293}$Ts, which readily $\alpha$ decays into its analog state in $^{289}$Mc. However, different to the $^{287}$Mc$\rightarrow^{283}$Nh decay discussed in connection with Fig. 8b, once electromagnetic decays within $^{293}$Ts reach its isomeric [510]1/2$^-$ level, this gives rise to second $\alpha$-decay branch. The predicted $Q_\alpha$ values are close to experiment. Calculations using the Skyrme energy density functional UNEDF1 suggest a practically degenerate 'ground-state pair' of [510]1/2$^-$ and [606]13/2$^+$ states, which will both $\alpha$ decay. The low-$\Omega$ negative-parity state has its low-lying analog Nilsson state to decay into, while the [606]13/2$^+$ level encounters some angular momentum and energy hindrance, such that an additional branching may occur. In conclusion, all three models rather support than reject the suggested presence of two parallel $\alpha$-decay sequences starting from $^{293}$Ts.



**Fig. 12** Evolution of set-ups towards the new LUNDIUM decay station. All drawings are generated from Geant4 simulations performed by Sarmiento [31]. **a** Positioning of germanium-detector crystals (coloured shapes) and the pixelated silicon-detector box (semi-transparent white) of the existing TASISpec arrangement [16]. **b** Set-up using four custom-made four-crystal COMPEX detectors [102] behind the box DSSD and one former EUROBALL cluster detector backing up the implantation DSSD. **c** Envisaged germanium detector configuration of the LUNDIUM chamber (cf. Fig. 14). The seven-crystal cluster is replaced by another COMPEX module, but with an electrical fourfold segmentation of each crystal. See text for details

## 6 From TASISpec to LUNDIUM

There are several components to further advance the nuclear spectroscopy opportunities for the heaviest elements. With the Lund group being engaged in the superheavy element research programme at GSI/FAIR, the new superconducting continuous-wave heavy-ion linear accelerator HELIAC [99] is going to deliver an increase in ion-beam rate and thus superheavy element production and observation rate. Provided that actinide targets can withstand the ion-beam related heating, also an increase in their thickness beyond 1 mg/cm$^2$ might become an option. However, given that these isotopically enriched materials are, besides being radioactive, extremely rare and precious, this is a major technological challenge (see, for example, [100] or Chap. 4 in [101]).

With these efforts and with the real cost of beam-time hours in mind, it is mandatory to also consider upgrades of the decay station. This can involve improvement of passive shielding and inclusion of active shielding to prevent unwanted background events in the silicon and germanium detectors. A higher granularity in the implantation DSSD pixelation allows for higher rates or prolonged correlation periods, respectively. Last but not least, a more compact germanium detector arrangement could increase $\alpha$-photon coincidence efficiency. The method must rely on the extraction of as much experimental spectroscopic information as possible for every single one of these extremely rarely produced superheavy nuclei.

These ideas are realized in the LUNDIUM decay station, a project financed by the Knut and Alice Wallenberg foundation. The major investment and technological development concerns a novel type of composited germanium detectors named COMPEX [102]. As sketched in Fig. 12a, TASISpec uses existing cluster (7 Ge crystals) and clover (4) germa-

nium detectors, which were available at GSI or made available through European networks. During experiments, the pixelated silicon cube detecting implanted superheavy elements and their $\alpha$ decay and fission is enclosed in a thin aluminium housing. The germanium detectors are thus *outside* the dilute helium atmosphere of the gas-filled separator TASCA. This also means that low-energy photon detection is impaired by unwanted material causing significant loss of photon detection efficiency – in particular for superheavy-element $L$ X-rays at 30–35 keV (cf. Fig. 13). Despite the close proximity to the silicon cube, there is still a distance of a few centimetres between silicon detectors and germanium crystals. Nevertheless, TASISpec reaches $\approx 40\%$ efficiency for $K$ X-rays [16,31].

Several Geant4 simulations investigating different germanium set-ups were conducted and led to configurations drawn in Fig. 12b, c. Common for them is the replacement of the four old clover detectors with novel, custom-made COMPEX detectors. These comprise four $5 \times 5 \times 5$ cm$^3$ cubes of encapsulated high-purity germanium crystals next to each other, and they use a modern type of electromechanical cryocooler [102]. Additionally, they can be placed *inside* the vacuum of a new LUNDIUM detection chamber, as illustrated in Fig. 14. No window at all besides the encapsulation is required, which maximizes low-energy photon detection. The difference in panels (b) and (c) is the type of germanium detector placed behind the implantation silicon detector: Panel (b), COMPEX-4, shows an existing cluster. In fact, with all germanium detectors still surrounding the TASISpec DSSD cube, this was the set-up used for the 'element 114 experiment' [21]. Positioning a fifth new COMPEX-type detector behind the implantation detector yields yet another decisive improve-
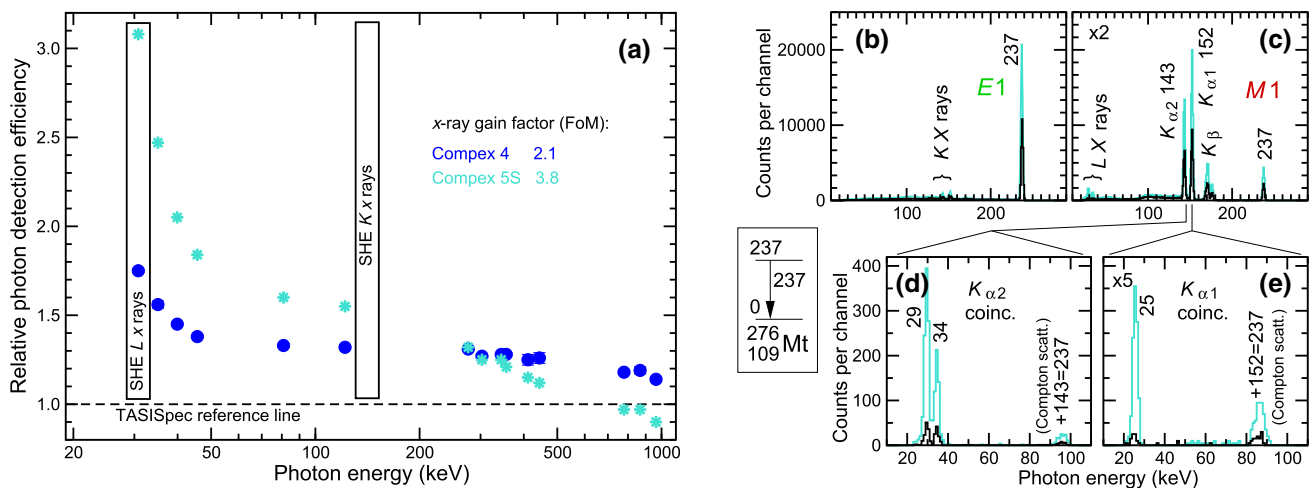
**Fig. 13** **a** Gain in photon detection efficiency for (low-energy) photons comparing the set-ups illustrated in Fig. 12b (Compex-4 plus Cluster, blue dots) and Fig. 12c (Compex-5S, cyan stars, LUNDIUM configuration) with the TASISpec version shown in Fig. 12a (dashed black line). Gamma-ray decays of excited superheavy elements are expected at energies of about 50–400 keV. Note the logarithmic scale on the x-axis with a focus on low-energy photon detection efficiencies. The X-ray gain factor, i.e., the figure-of-merit, is defined as the product of the gain in detection efficiency for a coincidence between $L$ and $K_\alpha$ X rays from a superheavy element. Panels **b**–**e** provide Geant4 simulations of photon spectra confronting the existing TASISpec set-up (black) with the Compex-5S system (cyan). The physics input is the simplified test case shown in the inset, namely an electromagnetic $E1$ (**b**) or $M1$ (**c**) 237-keV decay in meitnerium, $Z = 109$. Panels **d** and **e** show $L$ X rays in *coincidence* with $K_{\alpha2}$ and $K_{\alpha1}$ transitions, respectively, i.e., the decisive measure for a potential $Z$-fingerprint of a new superheavy element

ment in photon detection efficiency. In addition, electrical four-fold segmentation of each of the four crystals of this special COMPEX detector provides a significant improvement of spectral quality – this COMPEX-5S configuration became therefore the choice for the LUNDIUM set-up.

As mentioned earlier, the crux of the new concept, however, is to place the COMPEX detectors *in vacuum* directly behind the silicon detectors. The idea is to remove the end-cap of the cryostat housing, which is possible due to anticipated operation in vacuum. This is not possible with any of the existing detectors, and this is the essential improvement that will lead to the highly desirable increase in relative detection efficiency for low photon energies. In Fig. 13a the relative gain in efficiency as a function of photon energy is shown with respect to the existing TASISpec (dashed black horizontal line). The data points in Fig. 13a are derived from comprehensive Geant4 simulations [31] of $^{133}$Ba and $^{152}$Eu source ions implanted into the silicon detector with a depth and position profile representative of superheavy element experiment conditions. Overall, an increase in relative efficiency of $\epsilon_{K,rel} = 1.2$–$1.3$ at superheavy element $K$ X-ray energies and $\epsilon_{L,rel} = 1.7$–$1.8$ at $L$ X-ray energies is achieved for Compex-4, as shown by the blue circles in Fig. 13a. The product of those two numbers, $F = \epsilon_{K,rel} \cdot \epsilon_{L,rel} \sim 2.1$ for Compex-4 with respect to $F_0 = 1.0$ for TASISpec, may serve as the spectroscopic figure-of-merit of a given detector configuration. It represents to first order the increase in performance for detecting a coincidence between subsequent atomic $K_\alpha$ and

a $L$ $x$ ray following an electromagnetic decay of an excited nuclear state by inner conversion. With fluorescence yields [103,104] of more than 90% and 50%, respectively, the *coincident* observation of two X-ray fingerprinting energies is considered to provide the best possible evidence for the element number, $Z$, on (very) few-event statistics, based on the spectral analysis on the right hand side of Fig. 13.

Closing in with a fifth COMPEX detector right behind the implantation silicon detector implies that each of its four germanium crystals covers a rather large solid angle. This gives rise to a problem: possible energy summing due to the simultaneous detection of more than one photon in the same crystal. For instance, instead of measuring a 35-keV $L$ X-ray in one crystal and a coincident 140-keV $K_\alpha$ X-ray in a second crystal, a sum of 175 keV would be registered in one of the closed-in crystals. In more general terms, summing leads to unwanted, spurious peaks at summed energies of intense photon transitions of the respective source and has to be kept to a reasonable minimum. Therefore, a fourfold electrical segmentation of each of the four crystals of COMPEX module 5 is foreseen. The figure-of-merit increases to $F = 3.8$ for Compex-5S.

On the right hand side of Fig. 13, Geant4 simulations of photon spectra show the order-of-magnitude increase of (X-ray) coincidence spectroscopy with Compex-5S (cyan) compared to TASISpec (black). The physics input to the simulations is the simplified test case shown in the inset, namely an electromagnetic $E1$ (b) or $M1$ (c) 237-keV decay in meitner-
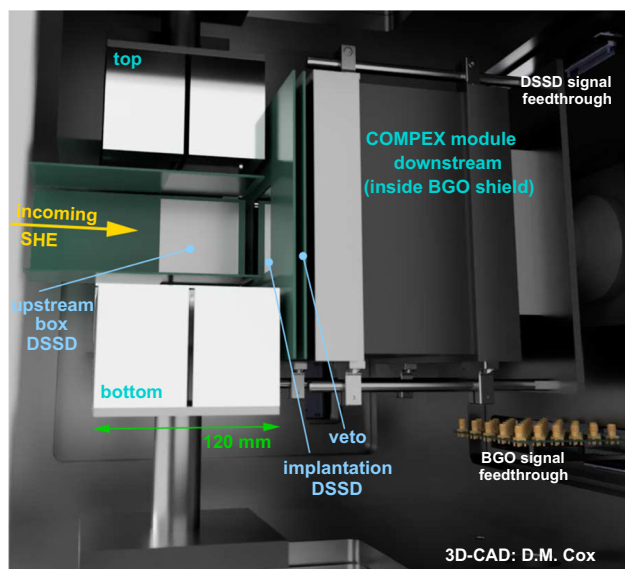
**Fig. 14** Rendered CAD-view into the new LUNDIUM vacuum chamber. The detector elements from the viewer's side and the BGO anti-Compton shields for the top and bottom COMPEX are removed. (Courtesy D.M. Cox)

ium. In case of $M1$ decay, the transitions are highly converted, i.e., instead of the $\gamma$-ray line at 237 [panel (b)], $K$-$x$ rays dominate the spectrum in panel (c). In line with increased relative efficiencies illustrated in Fig. 13(a) statistics are roughly doubled for Compex-5S vs. TASISpec. Most importantly, however, Compex-5S allows for X-ray *coincidence* spectroscopy: Panels (d) and (e) reveal a significant number of $L$ X rays in coincidence with $K_{\alpha 2}$ and $K_{\alpha 1}$ transitions, respectively. Such simultaneous X-ray energy measurements are unique for an element and thus the most decisive fingerprint for single- or few-event element determination. Chances are almost an order of magnitude larger for Compex-5S compared with TASISpec and reach several per cent for heavier and heavier superheavy elements.

Figure 14 provides a view into the new LUNDIUM chamber. The downstream segmented COMPEX module is hidden inside an anti-Compton shield assembled from 28 BGO crystals sized $19.1 \times 19.1 \times 100.0\,\mathrm{mm}^3$ [105]. Each of the four COMPEX detectors behind a box DSSD is protected against radiation from the beam direction with an anti-Compton assembly of twelve BGO crystals, so-called 'half-pockets' [105]. They are not shown in Fig. 14 for clarity. Compared with TASISpec, the strip pitch of the implantation DSSD is reduced from 1.8 to 1.0 mm, i.e., the number of pixelation is increased by more than a factor of 3. These detectors and implantation-veto correlations were subject to recent BSc thesis work [106,107]. There was no spectroscopic reason identified to increase the pixelation of the box DSSDs.

For the real LUNDIUM chamber, we expect the delivery of the segmented COMPEX module in 2022, likewise a few

vacuum pieces and BGO read-out electronics. It will then be subject to intense testing and characterization with standard $\alpha$, electron, and $\gamma$-ray sources.

## 7 Summary

To summarize, a brief overview of experimental and data analysis tools used in connection with TASISpec experiments has been presented. For more details, see in particular the PhD theses of Forsberg and Såmark-Roth [20,21]. Concerning envisaged improvements of detection, the LUNDIUM decay station employs novel concepts and technologies for compact high-resolution germanium detectors with unprecedentedly high detection efficiencies and precision placed directly behind the silicon detectors registering superheavy ion implantation and their charged-particle decays. The hope is to provide a spectroscopy set-up which ensures improved direct access to the nuclear structure of the heaviest man-made atomic nuclei, as well as X-ray fingerprinting their atomic number.

Concerning element discovery, alternative but statistically sound possible links between decay chains of $^{293}$Ts and $^{289}$Mc have been suggested. Clearly, more systematic data of spectroscopic quality is required. Coincidences between $\alpha$ particles and electrons or photons are likely to add important additional information to finally unravel the tangles of these chains.

Spectroscopic results on superheavy nuclei have been obtained which are capable of benchmarking nuclear structure models. These include several series of precise $Q_\alpha$ values across $Z = 114$, flerovium. The experimental findings imply that the next pronounced magic number beyond $Z = 82$, lead, is not at $Z = 114$, which is in line with many contemporary mean-field and beyond mean-field model calculations. Triaxial shapes, shape coexistence, and shape driving intruder orbitals are seemingly at play at $Z = 114$. High-$\Omega$ intruder orbitals are also involved in issuing a 237-keV $E1$ transition in $^{276}$Mt, the presence of which near the Fermi surface of $^{276}$Mt should be also be demonstrated by any nuclear structure model of relevance. The measured $\alpha$-decay fine-structure pattern in even-$Z$-odd-$N$ nuclei along the $^{289}$Fl decay chain is likely to engage a multitude of $\mathcal{N} = 6$ low-$\Omega$ positive-parity orbitals rather than $\mathcal{N} = 7$ high-$\Omega$ intruder orbitals. These are suggested to form an independent decay path. Starting from the somewhat provisional discussion of Figs. 6, 8, and 11, time has come to assess model and model parametrisations in greater detail along predicted single-particle states, collective states on top of these if applicable, and more elaborate $\alpha$-decay probabilities or hindrance factors. As a result, more robust predictions should emerge for experimentally unexplored territory.

The more recent spectroscopic achievements along flerovium decay chains were commented on in the referee report of [39]: "The wealth of physics discussion that a single event of this kind can generate is both stimulating and satisfying ... and demonstrates the robust promise for superheavy spectroscopy in the near future". Technical developments on beam intensity, target integrity, and detection efficiency should allow to "wring out tantalizing physics from compound nucleus production data where cross-sections are in the picobarn range".

**Note added in proofs:** Recently, the observation of additional 55 long and six short decay chains associated with isotopes of moscovium was reported [108]. The decay characteristics of the long chains are considered consistent with those previously assigned to start from $^{288}$Mc (cf. Fig. 7b and c and [69,71]), but an ∼50% a-decay branch of $^{268}$Db is newly proposed [108]. The decay characteristics of the six new short chains are detailed in their Supplemental Material [108].
In view of earlier assessments [64,69,71,72] (cf. Sec. 4), the new decay chains 1, 2 and 5, 6 are compliant with the nine decay chains shown in Fig. 7d, i.e., they can start from $^{288}$Mc and exit in $^{280}$Rg and $^{284}$Nh, respectively. Decay chains 3, 4 are candidates for the ensembles displayed in Fig. 7e or Fig. 7d. Overall, the scenarios discussed and suggested in Secs. 4 and 5 remain unchanged.

**Data Availability Statement** This manuscript has no associated data or the data will not be deposited. [Authors' comment: This review article relies on data already published elsewhere. See appropriate references throughout the article.]

## References

1. S.G. Nilsson, C.F. Tsang, A. Sobiczewski, Z. Szymański, S. Wycech, C. Gustafson, I.-L. Lamm, P. Möller, B. Nilsson, Nucl. Phys. A **131**, 1 (1969)
2. W.D. Meyers, W.J. Swiatecki, Ark. Fys. **36**, 343 (1967)
3. U. Mosel, W. Greiner, Z. Phys. **217**, 256 (1968)
4. K. Rutz, M. Bender, T. Bürvenich, T. Schilling, P.-G. Reinhard, J.A. Maruhn, W. Greiner, Phys. Rev. C **56**, 238 (1997)
5. A.V. Afanasjev, S. Frauendorf, Phys. Rev. C **71**, 024308 (2005)
6. J. Dobaczewski, A.V. Afanasjev, M. Bender, L.M. Robledo, Y. Shi, Nucl. Phys. A **944**, 388 (2015)
7. P.-H. Heenen, J. Skalski, A. Staszczak, D. Vretenatr, Nucl. Phys. A **944**, 415 (2015)
8. P.-H. Heenen, B. Bally, M. Bender, W. Ryssens, Eur. Phys. J. Web Conf. **131**, 02001 (2016)
9. J.L. Egido, A. Jungclaus, Phys. Rev. Lett. **125**, 192504 (2020)
10. J.L. Egido, A. Jungclaus, Phys. Rev. Lett. **126**, 192501 (2021)
11. H.G.J. Moseley, Philos. Mag. **26**, 1024 (1913)
12. C.E. Bemis Jr., R.J. Silva, D.C. Hensley, O.L. Keller Jr., J.R. Tarrant, L.D. Hunt, P.F. Dittner, R.L. Hahn, C.D. Goodman, Phys. Rev. Lett. **31**, 647 (1973)
13. Y.T. Oganessian, V.K. Utyonkov, Rep. Prog. Phys. **78**, 036301 (2015)
14. Yu.Ts. Oganessian, V.K. Utyonkov, Nucl. Phys. A **944**, 62 (2015)
15. V.K. Utyonkov, Y. Oganessian, S. Dmitriev, M. Itkis, K. Moody, M. Stoyer, D. Shaughnessy, J. Roberto, K. Rykaczewski, J. Hamilton, Eur. Phys. J. Web Conf. **131**, 06003 (2016)
16. L.-L. Andersson, D. Rudolph, P. Golubev, R.-D. Herzberg, R. Hoischen, E. Merchán, D. Ackermann, Ch.E. Düllmann, K. Eberhardt, J. Even et al., Nucl. Instr. Meth. A **622**, 164 (2010)
17. A. Semchenkov, W. Brüchle, E. Jäger, E. Schimpf, M. Schädel, C. Mühle, F. Klos, A. Türler, A. Yakushev, A. Belov et al., Nucl. Instr. Meth. B **266**, 4153 (2008)
18. M. Schädel, Eur. Phys. J. D **45**, 67 (2007)
19. P. Golubev, A. Wendt, L. Scruton, J. Taprogge, D. Rudolph, P. Reiter, M.A. Bentley, V. Avdeichikov, P. Boutachkov, S.P. Fox et al., Nucl. Instr. Meth. A **723**, 55 (2013)
20. U. Forsberg, *Element 115*, PhD thesis, Lund University, ISBN-978-91-7623-813-4 (2016). https://portal.research.lu.se/en/publications/element-115
21. A. Såmark-Roth, *Spectroscopy along Decay Chains of Element 114, Flerovium*, PhD thesis, Lund University, ISBN-978-91-7895-836-8 (2021). https://portal.research.lu.se/en/publications/spectroscopy-along-decay-chains-of-element-114-flerovium/
22. U. Forsberg, P. Golubev, L.G. Sarmiento, J. Jeppsson, D. Rudolph, L.-L. Andersson, D. Ackermann, M. Asai, M. Block, Ch.E. Düllmann et al., Acta Phys. Pol. B **43**, 305 (2012)
23. K.E. Gregorich, Nucl. Instr. Meth. A **711**, 47 (2013)
24. M. Asai, F.P. Heßberger, A. Lopez-Martens, Nucl. Phys. A **944**, 308 (2015)
25. D. Ackermann, Nucl. Phys. A **944**, 376 (2015)
26. D. Ackermann, Ch. Theisen, Phys. Scr. **92**, 083002 (2017)
27. A. Lopez-Martens, K. Hauschild, and the GABRIELA collaboration, Eur. Phys. J. A **58**, 134 (2022)
28. U. Forsberg, D. Rudolph, P. Golubev, L.G. Sarmiento, A. Yakushev, L.-L. Andersson, A. Di Nitto, Ch.E. Düllmann, J.M. Gates, K.E. Gregorich et al., Eur. Phys. J. Web Conf. **66**, 02036 (2014)
29. A. Såmark-Roth, L.G. Sarmiento, D. Rudolph, J. Ljungberg, B.G. Carlsson, C. Fahlander, U. Forsberg, P. Golubev, I. Ragnarsson, D. Ackermann et al., Phys. Rev. C **98**, 044307 (2018)
30. D.M. Cox, A. Såmark-Roth, D. Rudolph, L.G. Sarmiento, C. Fahlander, U. Forsberg, P. Golubev, J.A.M. Heery, A. Yakushev, H.M. Albers et al., J. Phys. G Conf. Ser. **1643**, 012125 (2020)

31. L.G. Sarmiento, L.-L. Andersson, D. Rudolph, Nucl. Instr. Meth. A **667**, 26 (2012)

32. L.G. Sarmiento, D. Rudolph, U. Forsberg, P. Golubev, L.-L. Andersson, Proceedings of Science, PoS(X LASNPA)057 (2014)

33. L.G. Sarmiento, Eur. Phys. J. Web Conf. **131**, 05004 (2016)

34. Ch. Lorenz, *Quantum-state Selective Nuclear Decay Spectroscopy*, PhD thesis, Lund University, ISBN-978-91-7753-943-8 (2018). https://portal.research.lu.se/en/publications/quantum-state-selective-nuclear-decay-spectroscopy

35. Ch. Lorenz, L.G. Sarmiento, D. Rudolph, D.E. Ward, M. Block, F.P. Heßberger, D. Ackermann, L.-L. Andersson, M.L. Cortés, C. Droese et al., Phys. Rev. C **96**, 034315 (2017)

36. Ch. Lorenz, L.G. Sarmiento, D. Rudolph, P. Golubev, T. Eronen, D.A. Nesterenko, A. Kankainen, L. Canete, D.M. Cox, A. Fernandez et al., Phys. Rev. C **99**, 044310 (2019)

37. L.G. Sarmiento, T. Roger, J. Giovinazzo, B.A. Brown, B. Blank, D. Rudolph, A. Kankainen, H. Alvarez-Pol, A. Arokia Raj, P. Ascher et al., (to be published)

38. D. Rudolph, JPS Conf. Proc. **6**, 010026 (2015)

39. A. Såmark-Roth, D.M. Cox, D. Rudolph, L.G. Sarmiento, B.G. Carlsson, J.L. Egido, P. Golubev, J. Heery, A. Yakushev, S. Åberg et al., Phys. Rev. Lett. **126**, 032503 (2021)

40. D.M. Cox, A. Såmark-Roth, D. Rudolph, L.G. Sarmiento, J.L. Egido, P. Golubev, J. Heery, A. Yakushev, S. Åberg, H.M. Albers, et al., Phys. Rev. Lett (in press)

41. A. Såmark-Roth, D.M. Cox, D. Rudolph, L.G. Sarmiento, M. Albertsson, B.G. Carlsson, J.L. Egido, P. Golubev, J. Heery, A. Yakushev, et al., Phys. Rev. C (to be published)

42. J.M. Gates, Ch.E. Düllmann, M. Schädel, A. Yakushev, A. Türler, K. Eberhardt, J.V. Kratz, D. Ackermann, L.-L. Andersson, M. Block et al., Phys. Rev. C **83**, 054618 (2011)

43. Yu.Ts. Oganessian, V.K. Utyonkov, Yu.V. Lobanov, F.Sh. Abdullin, A.N. Polyakov, I.V. Shirokovsky, Yu.S. Tsyganov, G.G. Gulbekian, S.L. Bogomolov, B.N. Gikal et al., Phys. Rev. C **62**, 041604(R) (2000)

44. Yu.Ts. Oganessian, V.K. Utyonkov, Yu.V. Lobanov, F.Sh. Abdullin, A.N. Polyakov, I.V. Shirokovsky, Yu.S. Tsyganov, G.G. Gulbekian, S.L. Bogomolov, B.N. Gikal et al., Phys. Rev. C **69**, 054607 (2004)

45. Yu.Ts. Oganessian, V.K. Utyonkov, Yu.V. Lobanov, F.Sh. Abdullin, A.N. Polyakov, I.V. Shirokovsky, Yu.S. Tsyganov, G.G. Gulbekian, S.L. Bogomolov, B.N. Gikal et al., Phys. Rev. C **70**, 064609 (2004)

46. Yu.Ts. Oganessian, V.K. Utyonkov, Yu.V. Lobanov, F.Sh. Abdullin, A.N. Polyakov, I.V. Shirokovsky, Yu.S. Tsyganov, G.G. Gulbekian, S.L. Bogomolov, B.N. Gikal, et al., JINR preprint, E7-2004-160, pp. 1–28 (2004)

47. Ch.E. Düllmann, M. Schädel, A. Yakushev, A. Türler, K. Eberhardt, J.V. Kratz, D. Ackermann, M. Block, W. Brüchle, J. Dvorak et al., Phys. Rev. Lett. **104**, 252701 (2010)

48. S. Hofmann, S. Heinz, R. Mann, J. Maurer, J. Khuyagbaatar, D. Ackermann, S. Antalic, W. Barth, M. Block, H.G. Burkhard et al., Eur. Phys. J. A **48**, 62 (2012)

49. D. Kaji, K. Morita, K. Morimoto, H. Haba, M. Asai, K. Fujita, Z. Gan, H. Geissel, H. Hasebe, S. Hofmann et al., J. Phys. Soc. Jpn. **86**, 034201 (2017)

50. F.P. Heßberger, Eur. Phys. J. Web Conf. **131**, 02005 (2016)

51. T. Kibédi, M.B. Trzhaskovskaya, M. Gupta, A.E. Stuchbery, At. Data. Nucl. Data Sheets **98**, 313 (2012)

52. C. Qi, F.R. Xu, R.J. Liotta, R. Wyss, M.Y. Zhang, C. Asawatangtrakuldee, D. Hu, Phys. Rev. C **80**, 044326 (2009)

53. B.G. Carlsson, J. Rotureau, Phys. Rev. Lett. **126**, 172501 (2021)

54. Yu. Oganessian, J. Phys. G **34**, R165 (2007)

55. A. Yakushev, J.M. Gates, A. Türler, M. Schädel, Ch.E. Düllmann, D. Ackermann, L.-L. Andersson, M. Block, W. Brüchle, J. Dvorak et al., Inorg. Chem. **53**, 1624 (2014)

56. A. Yakushev, L. Lens, Ch.E. Düllmann, J. Khuyagbaatar, E. Jäger, J. Krier, J. Runke, H.M. Albers, M. Asai, M. Block, et al., Front. Chem. **10**, 976635 (2022)

57. S. Ćwiok, W. Nazarewicz, P.H. Heenen, Phys. Rev. Lett. **83**, 1108 (1999)

58. A.N. Kuzmina, G.G. Adamian, N.V. Antonenko, Phys. Rev. C **85**, 027308 (2012)

59. J.L. Egido, private communication

60. F. Barranco, R.A. Broglia, G.F. Bertsch, Phys. Rev. Lett. **60**, 507 (1988)

61. R.M. Clark, D. Rudolph, Phys. Rev. C **97**, 024333 (2018)

62. R.M. Clark, D. Rudolph, Phys. Rev. C (to be published)

63. D. Rudolph, U. Forsberg, P. Golubev, L.G. Sarmiento, A. Yakushev, L.-L. Andersson, A. Di Nitto, Ch.E. Düllmann, J.M. Gates, K.E. Gregorich et al., Phys. Rev. Lett. **111**, 112502 (2013)

64. U. Forsberg, D. Rudolph, L.-L. Andersson, A. Di Nitto, Ch.E. Düllmann, C. Fahlander, J.M. Gates, P. Golubev, K.E. Gregorich, C.J. Gross et al., Nucl. Phys. A **953**, 117 (2016)

65. Yu.Ts. Oganessian, F.Sh. Abdullin, S.N. Dmitriev, J.M. Gostic, J.H. Hamilton, R.A. Henderson, M.G. Itkis, K.J. Moody, A.N. Polyakov, A.V. Ramayya et al., Phys. Rev. C **87**, 014302 (2013)

66. Yu.Ts. Oganessian, V.K. Utyonkov, Yu.V. Lobanov, F.Sh. Abdullin, A.N. Polyakov, I.V. Shirokovsky, Yu.S. Tsyganov, G.G. Gulbekian, S.L. Bogomolov, A.N. Mezentsev et al., Phys. Rev. C **69**, 021601(R) (2004)

67. Yu.Ts. Oganessian, V.K. Utyonkov, S.N. Dmitriev, Yu.V. Lobanov, M.G. Itkis, A.N. Polyakov, Yu.S. Tsyganov, A.N. Mezentsev, A.V. Yeremin, A.A. Voinov et al., Phys. Rev. C **72**, 034611 (2005)

68. J.M. Gates, K.E. Gregorich, O.R. Gothe, E.C. Uribe, G.K. Pang, D.L. Bleuel, M. Block, R.M. Clark, C.M. Campbell, H.L. Crawford et al., Phys. Rev. C **92**, 021301(R) (2015)

69. D. Rudolph, U. Forsberg, L.G. Sarmiento, P. Golubev, C. Fahlander, Eur. Phys. J. Web Conf. **117**, 01001 (2016)

70. K.H. Schmidt, Eur. Phys. J. A **8**, 141 (2000)

71. D. Rudolph, L.G. Sarmiento, U. Forsberg, A.I.P. Conf, Proc. **1681**, 030015 (2015)

72. U. Forsberg, C. Fahlander, D. Rudolph, Eur. Phys. J. Web Conf. **131**, 02003 (2016)

73. J.M. Gates, G.K. Pang, J.L. Pore, K.E. Gregorich, J.T. Kwarsick, G. Savard, N.E. Esker, M. Kireeff Covo, M.J. Mogannam, J.C. Batchelder, et al., Phys. Rev. Lett. **121**, 222501 (2018)

74. Yue Shi, D.E. Ward, B.G. Carlsson, J. Dobaczewski, W. Nazarewicz, I. Ragnarsson, D. Rudolph, Phys. Rev. C **90**, 014308 (2014)

75. D. Rudolph, U. Forsberg, P. Golubev, L.G. Sarmiento, A. Yakushev, L.-L. Andersson, A. Di Nitto, Ch.E. Düllmann, J.M. Gates, K.E. Gregorich et al., J. Radioanal. Nucl. Chem. **303**, 1185 (2015)

76. D. Rudolph, U. Forsberg, P. Golubev, L.G. Sarmiento, A. Yakushev, L.-L. Andersson, A. Di Nitto, Ch.E. Düllmann, J.M. Gates, K.E. Gregorich et al., Acta Phys. Pol. B **45**, 263 (2014)

77. U. Forsberg, D. Rudolph, C. Fahlander, P. Golubev, L.G. Sarmiento, S. Åberg, M. Block, Ch.E. Düllmann, F.P. Heßberger, J.V. Kratz, A. Yakushev, Phys. Lett. B **760**, 293 (2016)

78. A.N. Kuzmina, G.G. Adamian, N.V. Antonenko, Phys. Rev. C **85**, 017302 (2012)

79. P. Jachimowicz, M. Kowal, J. Skalski, Phys. Rev. C **89**, 024304 (2014)

80. A. Parkhomenko, A. Sobiczewski, Acta Phys. Pol. **35**, 2447 (2004)

81. A. Sobiczewski, Phys. Scr. **89**, 054014 (2014)

82. Yu.Ts. Oganessian, F.Sh. Abdullin, P.D. Bailey, D.E. Benker, M.E. Bennett, S.N. Dmitriev, J.G. Ezold, J.H. Hamilton, R.A. Henderson, M.G. Itkis et al., Phys. Rev. Lett. **104**, 142502 (2010)
83. Yu.Ts. Oganessian, F.Sh. Abdullin, P.D. Bailey, D.E. Benker, M.E. Bennett, S.N. Dmitriev, J.G. Ezold, J.H. Hamilton, R.A. Henderson, M.G. Itkis et al., Phys. Rev. C **83**, 054315 (2011)
84. Yu.Ts. Oganessian, F.Sh. Abdullin, C. Alexander, J. Binder, R.A. Boll, S.N. Dmitriev, J. Ezold, K. Felker, J.M. Gostic, R.K. Grzywacz et al., Phys. Rev. Lett. **109**, 162501 (2012)
85. Yu.Ts. Oganessian, F.Sh. Abdullin, C. Alexander, J. Binder, R.A. Boll, S.N. Dmitriev, J. Ezold, K. Felker, J.M. Gostic, R.K. Grzywacz et al., Phys. Rev. C **87**, 054621 (2013)
86. J. Khuyagbaatar, A. Yakushev, Ch.E. Düllmann, D. Ackermann, L.-L. Andersson, M. Asai, M. Block, R.A. Boll, H. Brand, D.M. Cox et al., Phys. Rev. Lett. **112**, 172501 (2014)
87. J. Khuyagbaatar, A. Yakushev, Ch.E. Düllmann, D. Ackermann, L.-L. Andersson, M. Asai, M. Block, R.A. Boll, H. Brand, D.M. Cox et al., Phys. Rev. C **99**, 054306 (2019)
88. J.B. Roberto, C.W. Alexander, R.A. Boll, J.D. Burns, J.G. Ezold, L.K. Felker, S.L. Hogle, K.P. Rykaczewski, Nucl. Phys. A **944**, 99 (2015)
89. K.P. Rykaczewski, J.B. Roberto, N.T. Brewer, Eur. Phys. J. Web Conf. **131**, 05005 (2016)
90. L. Öhrström, J. Reedijk, Pure Appl. Chem. **88**, 1225 (2016)
91. S.C. Burdette, P. Ball, K. Day, E.R. Scerri, B.F. Thornton, Nat. Chem. **8**, 283 (2016)
92. K. Gregorich, Eur. Phys. J. Web Conf. **131**, 06002 (2016)
93. K. Chapman, *Superheavy: Making and Breaking the Periodic Table*, (Bloomsbury Sigma, 2019)
94. E.R. Scerri, *The Periodic Table: Its Story and Its Significane*, (Oxford University Press, 2nd Edition, 2019)
95. U. Forsberg, D. Rudolph, L.-L. Andersson, A. Di Nitto, Ch.E. Düllmann, J.M. Gates, P. Golubev, K.E. Gregorich, C.J. Gross, R.-D. Herzberg, et al., arXiv:1502.03030v1 [nucl-exp], February 2015. https://arxiv.org/pdf/1502.03030.pdf
96. Yu.Ts. Oganessian, F.Sh. Abdullin, S.N. Dmitriev, J.M. Gostic, J.H. Hamilton, R.A. Henderson, M.G. Itkis, K.J. Moody, A.N. Polyakov, A.V. Ramayya et al., Phys. Rev. Lett. **108**, 022502 (2012)
97. D. Rudolph, U. Forsberg, Ch.E. Düllmann, P. Golubev, F.P. Heßberger, J.V. Kratz, L.G. Sarmiento, A. Yakushev, D. Ackermann, L.-L. Andersson, et al., GSI-SR2014-MU-NUSTAR-SHE-C-02, GSI Report 2015-1
98. A. Sobiczewski, Acta Phys. Pol. **41**, 157 (2010)
99. M. Schwarz, S. Yaramyshev, K. Aulenbacher, W. Barth, M. Basten, M. Busch, C. Burandt, T. Conrad, F. Dziuba, V. Gettmann et al., Nucl. Instr. Meth. A **951**, 163044 (2020)
100. J. Runke, Ch.E. Düllmann, K. Eberhardt, P.A. Ellison, K.E. Gregorich, S. Hofmann, E. Jäger, B. Kindler, J.V. Kratz, J. Krier et al., J. Radioanal. Rad. Nucl. Chem. **299**, 1081 (2014)
101. Ch.E. Düllmann, M. Block, F.P. Heßberger, J. Khuyagbaatar, B. Kindler, J.V. Kratz, B. Lommel, G. Münzenberg, V. Pershina, D. Renisch, M. Schädel, A. Yakushev, Radiochim. Acta **110**, 417 (2022)
102. A. Såmark-Roth, D.M. Cox, J. Eberth, P. Golubev, D. Rudolph, L.G. Sarmiento, G. Tocabens, M. Ginsz, B. Pirard, P. Quirin, Eur. Phys. J. A **56**, 141 (2020)
103. T.A. Carlsson, C.W. Nestor Jr., F.B. Malik, T.C. Tucker, Nucl. Phys. A **135**, 57 (1969)
104. T.A. Carlsson, C.W. Nestor Jr., F.B. Malik, T.C. Tucker, At. Data Nucl. Data Tables **19**, 153 (1977)
105. Y. Hrabar, L.G. Sarmiento, P. Golubev, D.M. Cox, D. Rudolph, Nucl. Instr. Meth. A (to be published)
106. E. Kosta, *Dead layer determination for the new implantation detector of the LUNDIUM decay station*, BSc thesis, Lund University (2022). https://lup.lub.lu.se/student-papers/search/publication/9074244
107. T. Sayed, *Assessment of the Capability for Vetoing Beta-Decay Events in the Lundium Decay Station*, BSc thesis, Lund University (2022). https://lup.lub.lu.se/student-papers/search/publication/9074978
108. Yu.Ts. Oganessian, V.K. Utyonkov, N.D. Kovrizhnykh, F.Sh. Abdullin, S.N. Dmitriev, D. Ibadullayev, M.G. Itkis, D.A. Kuznetsov, O.V. Petrushkin, A.V. Podshibiakin, et al., Phys. Rev. C **106**, L031301 (2022)